Single-cell profiling reveals monocyte mitochondrial dysfunction in patients with cirrhosis progressing to acute-on-chronic liver failure

Authors:

Theresa H. Wirtz[1†], Sara Palomino-Echeverria[2,3,4†*], Maike R. Pollmanns[1], Estefanía Huergo[2], Felix Schreibing[5], Johanna Reißing[1], Cristina Sánchez-Garrido[6], Cristina López-Vicario[6,7,8], Ana M. Aransay[8,9], Maurizio Baldassare[10], Giacomo Zaccherini[10,11], Enrico Pompili[10,11], Martin Schulz[12], Frank E. Uschner[12], Sabine Klein[12], Wenyi Gu[12], Robert Schierwagen[12], Shantha Valainathan[13], Annabelle Verbeeck[13], Daniela Campion[14], Ilaria Giovo[14], Kai Markus Schneider[1, 15,16,17], Alexander Koch[1], Rafael Kramann[5,18], Tony Bruns[1], Narsis Kiani[19], Linsey Stiles[20,21], Paolo Caraceni[10,22], Carlo Alessandria[14], Richard Moreau[6,13,23], Jonel Trebicka[6,12], Joan Clària[6,7,8,24], Núria Planell[25*], Pierre-Emmanuel Rautou[6,13,18#*], Christian Trautwein[1,26,27#*], David Gomez-Cabrero[2,28#*]

Affiliations:

[1]Medical Department III, University Hospital RWTH Aachen, Aachen, Germany

[2]Translational Bioinformatics Unit (TransBio), Navarrabiomed, Navarra Health Department (CHN), Public University of Navarra (UPNA), Navarra Institute for Health Research (IdiSNA), Pamplona, Spain

[3]Research Program in Systems Oncology, University of Helsinki, Helsinki, Finland

[4]Institute for Molecular Medicine Finland, Helsinki Institute for Life Sciences, University of Helsinki, Helsinki, Finland

[5]Department of Medicine 2 (Nephrology, Rheumatology, Clinical Immunology and Hypertension), RWTH Aachen University, Medical Faculty, Aachen, Germany

[6]European Foundation for the Study of Chronic Liver Failure (EF CLIF) and Grifols Chair, Barcelona, Spain

[7]Biochemistry and Molecular Genetics Service, Hospital Clinic-IDIBAPS, Barcelona, Spain

[8]CIBERehd, Madrid, Spain

[9]Center for Cooperative Research in Biosciences (CIC bioGUNE), Derio, Bizkaia, Spain

[10]Unit of Semeiotics, Liver and Alcohol-related Diseases, IRCCS Azienda Ospedaliero-Universitaria di Bologna, Bologna, Italy

[11]Department of Medical and Surgical Sciences (DIMEC), Alma Mater Studiorum, University of Bologna, Bologna, Italy

[12]Department of Internal Medicine B, University Hospital Muenster, Muenster, Germany

[13]AP-HP, Hôpital Beaujon, Service d´Hepatologie, DMU DIGEST, Centre de Référence des Maladies Vasculaires du Foie, FILFOIE, ERN RARE-LIVER, Clichy, France

[14]Division of Gastroenterology and Hepatology, A.O.U. Città della Salute e della Scienza di Torino, Torino, Italy

[15]Department of Medicine 1, University Hospital Carl Gustav Carus Dresden, Technische Universität (TU), Dresden, Germany

[16]Center for Regenerative Therapies Dresden (CRTD), Technische Universität (TU), Dresden, Germany

[17]Else Kroener Fresenius Center for Digital Health, Medical Faculty Carl Gustav Carus, TUD Dresden University of Technology, Dresden, Germany

[18]Department of Internal Medicine, Nephrology and Transplantation, Erasmus Medical Center, Rotterdam, The Netherlands

[19]Algorithmic Dynamics lab, Department of Oncology-Pathology, Karolinska Institutet, Solna, Sweden

[20]Department of Molecular and Medical Pharmacology, University of California, Los Angeles, California, USA
[21]Department of Medicine, Endocrinology, David Geffen School of Medicine, University of California, Los Angeles, California, USA
[22]IRCCS Azienda Ospedaliera-Universitaria di Bologna, Bologna, Italy
[23]Université Paris-Cité, Inserm, Centre de recherche sur l´inflammation, UMR 1149, Paris, France
[24]Department of Biomedical Sciences, University of Barcelona, Spain
[25]Universidad de Navarra, Centro de Investigación Médica Aplicada (CIMA), Computational Biology Program, Instituto de Investigación Sanitaria de Navarra (IdiSNA), Pamplona, Spain
[26]Leibniz Research Centre for Working Environment and Human Factors at the TU Dortmund (IfADo), Dortmund, Germany
[27]Liver Center, Department of Gastroenterology, Hepatology and GI-Oncology, Klinikum Stuttgart, Stuttgart, Germany
[28]Bioscience Program, Biological and Environmental Sciences and Engineering Division (BESE), King Abdullah University of Science and Technology KAUST, Thuwal, Saudi Arabia

†: These authors contributed equally to this work and share first authorship. Either name may be listed first when citing.
#: These authors contributed equally to this work and share last authorship.
*: **Corresponding authors:** sara.palominoecheverria@helsinki.fi, nplanellpic@unav.es, pierre-emmanuel.rautou@inserm.fr, trautwein.christian@gmx.net, david.gomez.cabrero@navarra.es

Key words: acute decompensation, acute-on-chronic liver failure, cirrhosis, prognosis, scRNA-seq, CITE-seq, monocytes, CD14, energy metabolism

Abstract

Patients with acute decompensation (AD) of cirrhosis face a high risk of acute-on-chronic liver failure (ACLF), a syndrome linked to multiple organ failure and high mortality. This study analyzed peripheral blood mononuclear cells (PBMCs) using single-cell technologies to explore their role in patient outcomes. Blood samples from 15 healthy donors and 63 AD patients were prospectively collected at hospital admission across five European centers, with patients monitored for 90 days. CITE-seq was performed on PBMCs from 4 controls and 16 patients representing different disease trajectories. A rise in classical monocytes, particularly subcluster "C2," was noted in patients progressing to ACLF. This subset showed impaired energy metabolism, with reduced oxidative phosphorylation and ATP production. Notably, genes coding for Complex IV of the respiratory chain were significantly downregulated. In two large prospective international cohorts (PREDICT, n=689; ACLARA, n=521), we observed that a gene signature from C2 was elevated in patients with cirrhosis with bacterial infections, ACLF, and in non-survivors. Functional validation of our findings was performed using respirometry analyses in an independent AD cohort, specifically evaluating mitochondrial function in the total classical monocyte population. A progressive decline in Complex IV-driven oxygen consumption rate (OCR) was observed in pre-ACLF patients. In conclusion, we identified and validated that patients with AD having a poor outcome are characterized by a subpopulation of monocytes with impaired energy metabolism. This cell population might contribute to the transition from AD to ACLF.

84 ## Teaser

85 A unique monocyte subset with metabolic dysfunction is associated with disease progression in
86 patients with acute decompensation of cirrhosis.

87 # Introduction

88 Acute decompensation (AD) is the most frequent cause of hospitalization among individuals diagnosed
89 with cirrhosis (1). It involves the emergence of one or more clinically relevant complications, such as
90 ascites, hepatic encephalopathy, or gastrointestinal bleeding (2–4). Patients with AD are at high risk
91 of developing acute-on-chronic liver failure (ACLF) – a clinical syndrome marked by the acute
92 deterioration of liver function in individuals with AD accompanied by the failure of one or more major
93 organs or systems (5,6). Depending on the severity and number of organ failures, ACLF is associated
94 with poor short-term mortality ranging from 15% to 80% (7).

95 The transition from decompensated cirrhosis to ACLF is a dynamic and multifactorial process driven
96 by a complex interplay of systemic inflammation (SI), immune dysfunction, and organ crosstalk (8,9).
97 Significant progress has been made in understanding the underlying pathophysiological mechanisms
98 as well as identifying the pivotal mediators that initiate and regulate these processes. Particularly, SI
99 was identified to gradually increase with the progression of portal hypertension and to induce organ
100 dysfunction as part of ACLF transition (10,11). Respective studies have identified increased circulating
101 levels of pro-inflammatory cytokines and the activation of innate immune pathways, including Toll-
102 like receptor (TLR) signaling, as key contributors (12,13). Furthermore, the translocation of microbial
103 products from the gut into systemic circulation, a consequence of intestinal barrier dysfunction, has
104 been implicated in exacerbating SI and immune activation (14). In parallel, cellular studies have
105 revealed immune cells to exhibit phenotypic and functional alterations that promote SI and impair
106 immune response. Dysfunctional neutrophils and monocytes have been identified to impair innate
107 immunity and increase susceptibility to bacterial infection – a common trigger of ACLF (15–17).
108
109 Despite these advances, the relative contributions of different immune cell subsets during disease
110 progression are incompletely defined, and the identification of functional cellular states associated
111 with ACLF development remains an area of investigation. Single-cell technologies, including single-cell
112 RNA sequencing (scRNA-seq), have emerged as transformative tools for dissecting cellular
113 heterogeneity and capturing the dynamic immune landscape in complex diseases. Hence, recent
114 studies have used scRNA-seq to elucidate pathophysiological characteristics of peripheral immune
115 cells in patients with ACLF compared to healthy controls (18–21). They identified distinct
116 immunometabolic cellular states contributing to ACLF outcome, with the most significant changes in
117 pro-inflammatory monocytes and T-cells (18–21). However, those publications focused on patients
118 who already transitioned to ACLF. Yet, no prospective, high-resolution baseline analysis of functional
119 alterations of peripheral immune cells in patients with AD who subsequently develop ACLF is available.

120 We, therefore, conducted a prospective multicenter study involving patients admitted due to AD at
121 five different European centers. The aim of the study was to characterize the PBMCs at single-cell
122 resolution. Our data provide insights into changes within peripheral immune cell subpopulations
123 associated with AD progression, as well as molecular mechanisms driving ACLF development.

Results

Single-cell study cohort and sample description

In total, 63 patients with AD and 15 healthy controls were prospectively recruited in 5 European centers. After 90 days, patients were classified as having no readmission due to AD (SDC), readmission due to AD (UDC), or ACLF development within the first 28 days (pre-ACLF). Of those, 16 patients (6 SDC, 6 UDC, 4 pre-ACLF) and four healthy controls were selected for single-cell analysis (see Material and Methods; **Figure 1 A; Supplementary Figures 1**). Respective PBMC samples subsequently underwent CITE-seq; bulk RNA-seq on whole blood from the same patients was also performed (**Figure 1 B**). The median age at the time of hospital admission was 60 years in the SDC, 57 years in the UDC, and 74 years in the pre-ACLF group (**Table 1**; see end of the document). Of all patients, 75% were males, and 50% had been diagnosed with alcohol-related liver cirrhosis. Previous episodes of acute decompensation were common in the UDC (4/6 patients) and pre-ACLF (3/4 patients) groups. The primary reason for hospital admission in all groups was ascites. Bacterial infection was present in 2 out of 6 SDC patients, and spontaneous bacterial peritonitis (SBP) was evident in 2 out of 4 pre-ACLF patients. MELD and CLIF-C AD scores were significantly higher in the pre-ACLF group compared to the SDC and the UDC groups (20 and 59 points, respectively). Treatment at blood draw was not significantly different between the groups. All pre-ACLF patients developed ACLF during their first hospital admission. Within the pre-ACLF group, one patient died, and one patient underwent a liver transplant during follow-up. Additional baseline characteristics are presented in **Supplementary Tables 1, 2, and 3.**

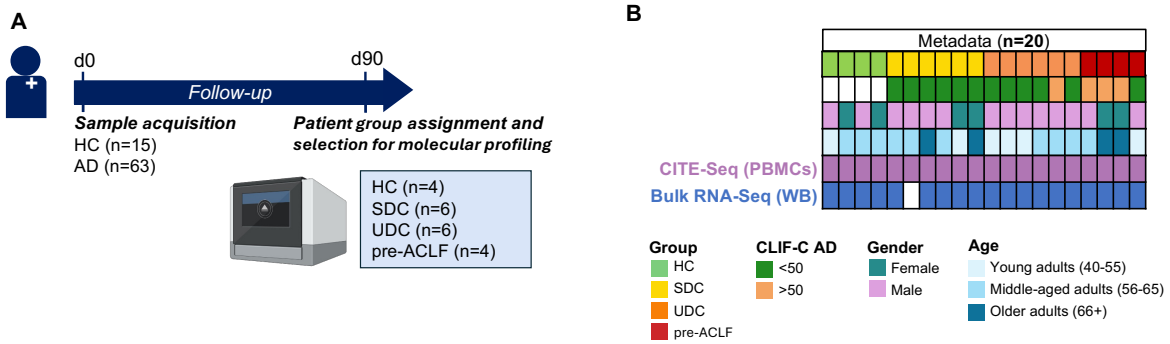

Figure 1. Study design.
(A) Schematic cartoon of the study design. PBMC samples from 63 patients admitted with AD and 15 HC were collected. After 90 days of follow-up (d90), AD patients were classified as SDC, UDC, or pre-ACLF due to their clinical course. Of those, 16 patients and 4 HC were selected for scRNA-seq analysis. **(B)** Representation of the multi-omics approach along with the associated clinical metadata, including study group, CLIF-C AD score, gender, and age. *Abbreviations:* AD, acute decompensation; HC, healthy controls; PBMCs, peripheral blood mononuclear cells; pre-ACLF, pre-acute-on-chronic liver failure; SDC, stable decompensated cirrhosis; UDC, unstable decompensated cirrhosis; WB, whole blood.

155 ***An increase in circulating classical monocytes is associated with ACLF development***

156 For the single-cell transcriptional analysis, 130,846 cells, with a median of 1,632 genes per cell, were
157 recovered from the 20 individuals included in this study (**Figure 1 A**). We identified 11 cell clusters
158 corresponding to classical monocytes, non-classical monocytes, CD4$^+$ T cells, CD8$^+$ T cells, B cells, NK
159 cells, MAIT cells, dendritic cells, regulatory T cells, dnT cells, and gdT cells (**Figure 2 A, Supplementary**
160 **Figures 2**). Cell annotation was confirmed by cell surface marker profiling (**Supplementary Figure 3 A,**
161 **B**).

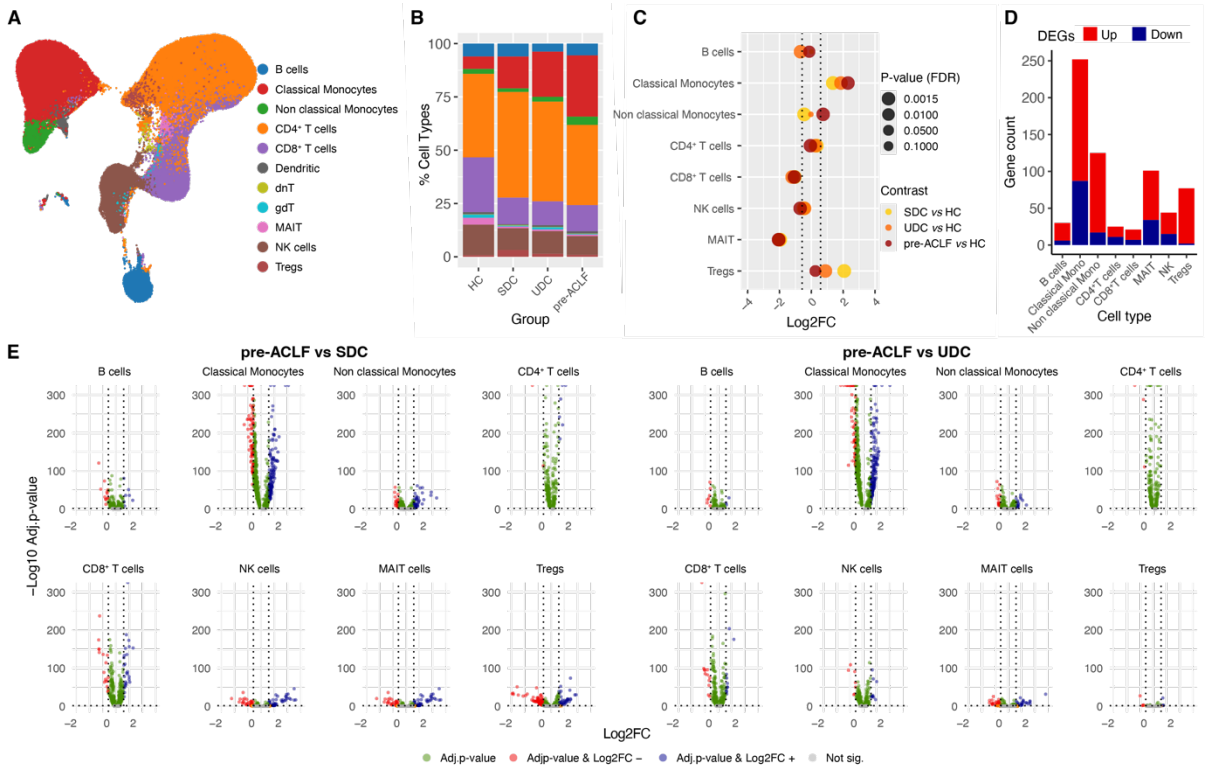

162

163 ***Figure 2. Single-cell transcriptional profiling of PBMCs from healthy controls and patients with SDC, UDC, and***
164 ***pre-ACLF.***
165 **(A)** UMAP projection of the 143,952 PBMCs analyzed, colored by the 11 detected cell populations. **(B)** Barplot
166 showing the variability of immune cell subsets between the different groups. **(C)** Cleveland plot showing the log2
167 fold-change for the eight main cellular subpopulations. For each cell type, pairwise comparisons were made:
168 SDC *vs*. HC (yellow), UDC *vs.* HC (orange), and pre-ACLF *vs.* HC (dark red). Cell types were considered differentially
169 expressed when the fold change (log2 FC; estimated using a bootstrapping confidence interval analysis) was >
170 0.58 (dashed vertical lines) and the adjusted p-value was < 0.05 (represented by the dot size; estimated using a
171 permutation analysis). **(D)** Sum of the number of DEGs across cell types; a gene is considered significant if
172 adjusted p-value < 0.05 (Benjamini-Hochberg) and absolute Fold Change > 1.5. **(E, F)** Volcano plots representing
173 the fold change (log2 FC) and statistical significance (adjusted p-value) for different immune cell populations: B
174 cells, classical monocytes, non-classical monocytes, CD4+ T cells, CD8+ T cells, NK cells, MAIT cells, and Tregs.
175 The x-axis shows the log2 FC, while the y-axis represents the -log10 of the adjusted p-values for each gene. Points
176 in red and blue indicate statistically significant changes (based on adjusted p-values) with positive or negative
177 log2FC, respectively, while gray points indicate non-significant changes. **E,** illustrates the comparison of pre-ACLF
178 against SDC, and **F,** illustrates the comparison of pre-ACLF against UDC. *Abbreviations:* AD, acute
179 decompensation; HC, healthy controls; NK cells, natural killer cells; MAIT cells, mucosal-associated invariant T
180 cells; PBMCs, peripheral blood mononuclear cells; pre-ACLF, pre-acute-on-chronic liver failure; SDC, stable
181 decompensated cirrhosis; Tregs, regulatory T cells; UDC, unstable decompensated cirrhosis.
182

183 To identify changes in cellular proportions associated with disease progression, we compared the cell
184 compositions of healthy controls, SDC, UDC, and pre-ACLF groups. We observed marked proportion
185 variations when investigating the most prevalent cell subtypes (those representing at least 1% of the
186 total cells) (**Figure 2 B, C**). As expected, we found a significant increase of classical monocytes in AD
187 patients compared to healthy controls, with pre-ACLF exhibiting the highest fold change, followed by
188 UDC and SDC. Non-classical monocytes also increased significantly in the pre-ACLF patients but to a
189 lesser extent. Regarding T cell populations, $CD8^+$ T cells in AD patients decreased compared to healthy
190 controls. Similar trends were observed in cell proportions derived from surface protein markers´ data
191 (**Supplementary Figure 3 C, D**).

192 Differential expression analysis (DEA) was performed to examine transcriptional changes within each
193 cell population among AD patients and healthy controls. We identified varying numbers of
194 differentially expressed genes (DEGs) in each cell type and contrast (SDC vs. healthy controls, UDC vs.
195 healthy controls, pre-ACLF vs. healthy controls) (**Figure 2 D**). Classical monocytes showed the highest
196 number of DEGs in both the total of all comparisons and each comparison individually. In detail, pre-
197 ACLF comparisons with SDC and UDC, respectively, showed that they exhibited the highest number of
198 DEGs, especially in classical monocytes (**Figure 2 E and Supplementary Figure 4**).

199 Overall, we identified perturbations in the peripheral immune cell landscape in AD patients compared
200 to healthy controls, with a notable accentuation of the monocytic population, especially in the pre-
201 ACLF patients.

202 ***Identification of a classical monocyte subpopulation associated with AD progression***

203 Given the observed alterations in cell proportion and gene expression of classical monocytes in AD
204 patients compared to healthy controls, we next explored their role in disease progression by
205 identifying distinct classical monocytic subpopulations. To this end, we applied unsupervised
206 clustering to the classical monocytes, identifying three major cell subclusters labelled as C0, C1, and
207 C2 (**Figure 3 A**). C0 constituted the highest proportion of classical monocytes, followed by C1 and C2.

208 Next, we investigated differences in the identified monocytic subclusters within the four clinical
209 groups. Similar to the overall monocyte population, all three monocyte subpopulations were
210 increased in AD patients compared to healthy controls (**Figure 3 B, Supplementary Figure 5**).
211 Specifically, C0 increased significantly in all AD groups, C1 was significantly enriched in UDC and pre-
212 ACLF patients, and C2 only in the pre-ACLF patients (**Figure 3 C**). Interestingly, within the pre-ACLF
213 group, the proportions of C1 and C2 monocytes increased according to the latency of ACLF onset
214 (**Figure 3 B)**. To further investigate the dynamic processes underlying the monocyte compartment,
215 trajectory analysis was complemented, which identified a continuous process from C0 to C2, with C1
216 representing a transitional state between C0 and C2 monocytes (**Figure 3 D**).

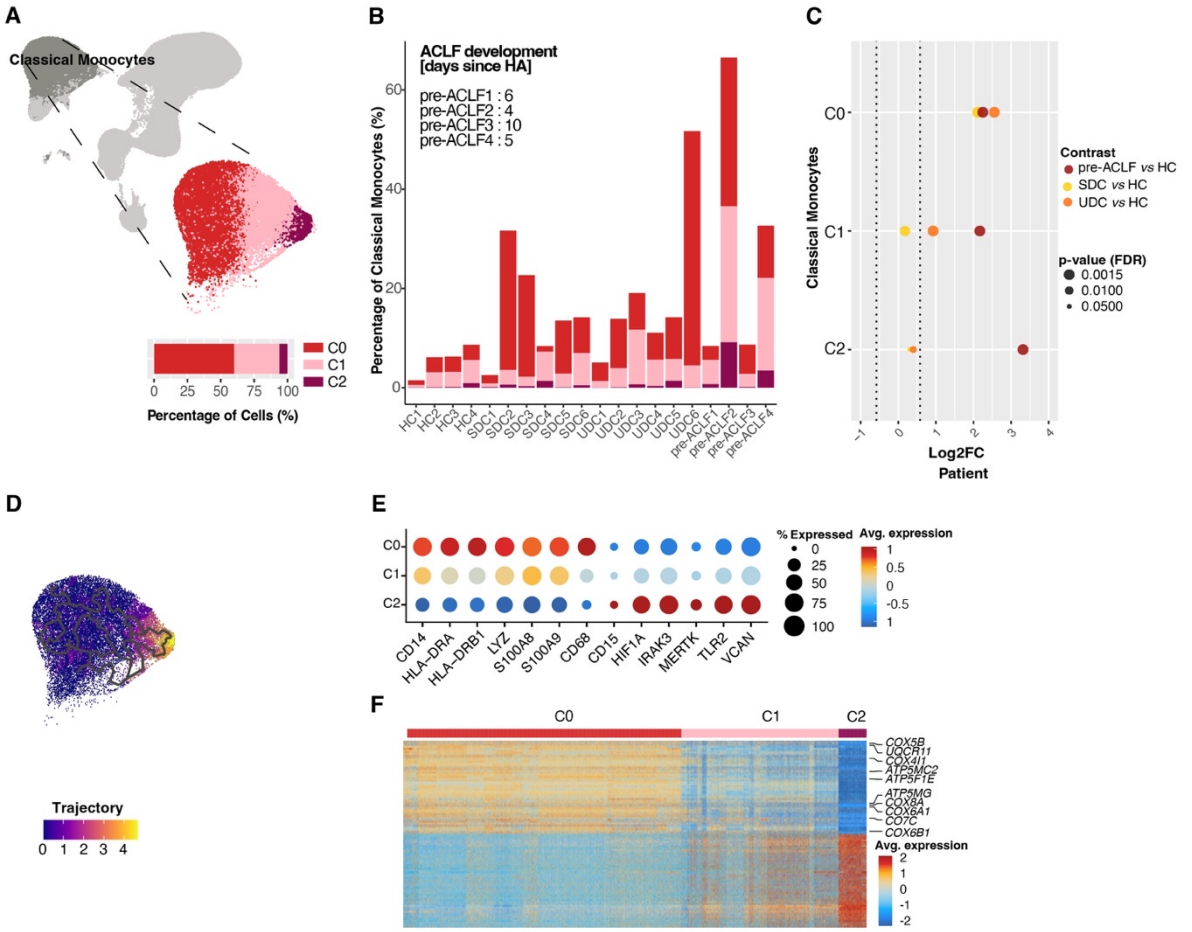

Figure 3. Identification of a classical monocyte subpopulation associated with ACLF development.
(A) UMAP of all cell types with a zoom on classical monocytes with cells colored based on the subclusters C0, C1, and C2. **(B)** Relative percentages of each monocyte subcluster in each individual. **(C)** Cleveland plot showing the log2 fold-change in cell subtype prevalence for the 3 monocyte subclusters. For each subcluster, pairwise comparisons were made: SDC vs. HC, UDC vs. HC, and pre-ACLF vs. HC. Log2FC and FDR were estimated, respectively, using bootstrapping and permutation analysis. **(D)** UMAP with the pseudo-time trajectory on classical monocytes subclusters using Monocle3. **(E)** Dot plot indicating the expression of selected genes in each monocytic subcluster. **(F)** Heatmap displaying the scaled expression values of the top 50 up and downregulated genes in each subcluster. Please find extensive gene annotation in Supplementary Figure 10. *Abbreviations:* Avg, average; HC, healthy controls; Log2FC, logarithmic 2 Fold Change; pre-ACLF, pre-acute-on-chronic liver failure; SDC, stable decompensated cirrhosis; UDC, unstable decompensated cirrhosis.

Transcriptional profiling of C2 monocytes

In the next step, we aimed to elucidate the functional and pathophysiological characteristics of the C2 subset. We first explored the transcriptional profile of monocytic markers with known biological function in these cells (**Figure 3 E**). In contrast to the C0 subset, we observed lower expression of *CD14*, as well as of genes encoding HLA-DR subunits (*HLA-DRA*) or isoforms (*HLA-DRB1*) in the C2 cluster. Moreover, the expression of genes encoding pro-inflammatory mediators from the S100 protein family, as well as antibacterial agents such as lysozyme (*LYZ*), were decreased within the C2 subset. In contrast, genes encoding proteins involved in regulating inflammation and infection, such as MERTK, VCAN, IRAK3, HIF1α, and TLR2, showed increased expression compared to C0. The expression of *CD15* was also higher in C2. C1 monocytes showed an intermediate state between C0 and C2.

241 Given the immunoregulatory phenotype of C2 monocytes, we considered whether this population
242 might share features with endotoxin-tolerant monocytes, previously described in patients with
243 cirrhosis. To address this, we compared the transcriptomic profile of C2 to a published in vivo dataset
244 of sepsis-associated monocytes (MS1) (22), which serve as a reference for endotoxin-tolerant
245 monocyte states arising in severe systemic inflammation. Interestingly, the transcriptional overlap
246 between C2 and MS1 monocytes was limited, and no significant enrichment of the MS1 signature was
247 observed in C2 (**Supplementary Figure 6 A, B, C**).

248 We then performed DEA to characterize transcriptional changes between the C2 subcluster and the
249 C0 and C1 subclusters. Analysis of the top 100 up- and downregulated genes confirmed the
250 intermediate state of C1 (**Figure 3 F, Supplementary Figure 7)**. Interestingly, the upregulated genes
251 illustrated a rather heterogeneous biological pattern. In contrast, among the most downregulated
252 genes, we observed several genes that encode different proteins/enzymes involved in processes
253 relevant to energy production and metabolism. These genes included ATP-production genes (i.e. gene:
254 *ATP5F1E*/protein: ATP synthase F1 subunit epsilon**;** *ATP5MG*/ATP synthase membrane subunit g) and
255 oxidative phosphorylation genes (*UQCR11*/ubiquinol-cytochrome c reductase, complex III sub-unit XI;
256 *COX7C*/cytochrome c oxidase subunit 7C; *COX8A*/cytochrome c oxidase subunit 8A). In total, three
257 genes encoding ATP synthase/Complex V membrane subunits and six encoding cytochrome c
258 oxidase/Complex IV subunits were among the 50 most downregulated genes in the C2 subset
259 compared to C0/C1. Moreover, among the downregulated genes, we found numerous S100 proteins
260 described as important regulators of stress and inflammatory responses (**Supplementary Figure 7**).

261 Given the transcriptional profile of C2 classical monocytes, showing a decreased expression of the
262 surface receptor *HLA-DR*, we wondered whether this translates at the protein level. Hence, we
263 assessed the HLA-DR profile by flow cytometry on classical monocytes enriched from PBMCs from the
264 same AD and healthy control individuals**.** To analyze differences of the HLA-DR expression between
265 the groups, the delta of the mean fluorescence intensity (ΔMFI) of HLA-DR was calculated by
266 subtracting the mean MFI count in the SDC group from single MFI counts in the four study groups.
267 Even if the entire population of classical monocytes was considered in this approach, we still observed
268 a statistical tendency towards a decreased relative HLA-DR expression in patients with pre-ACLF
269 (**Supplementary Figure 8**).

270 Thus, we identified a distinct monocytic whose abundance is associated with future ACLF
271 development. This subcluster is predominantly characterized by decreased expression of genes
272 involved in cellular energy supply.
273

274 ***Functional characterization of the classical monocyte subset C2***

275 To better define the biological functions of the identified monocyte subsets, we conducted gene set
276 enrichment analysis (GSEA) comparing C2 and C0, with C1 as an intermediate state. Our analysis
277 revealed a significant global downregulation of pathways related to energy metabolism, including
278 "*oxidative phosphorylation (OXPHOS)*" and "*aerobic respiration*" – both representing the most overall
279 regulated pathways in this data set–, as well as "*ATP biosynthetic process*" in the C2 subset (**Figure 4**
280 **A** and **Supplementary Table 4**). Additionally, we examined how these biological processes were
281 regulated across the different subclusters (C0, C1, and C2) (**Figure 4B**) and patient subgroups (healthy

controls, SDC, UDC, and pre-ACLF) (**Figure 4C**). Importantly, our findings indicated that C2 had significantly lower signature scores than C0 and C1 subclusters independently of the clinical course.

Since bacterial infection represents a complication of cirrhosis-associated immune dysfunction and a critical driver of ACLF progression, we also examined pathways related to the immune response in the C2 monocytes (**Figure 4 D**). Although no significantly regulated pathways were identified based on adjusted p-value, we observed a tendency towards a reduced activity of pathways related to the immune response in C2 monocytes. Among them, we identified "*positive regulation of inflammatory response*", "*defense response to bacterium*", and "*cytokine production*" (**Figure 4 D** and **Supplementary Table 4**).

Thus, C2 monocytes display a significant disruption in pathways related to cellular energy supply and a tendency towards a dysfunctional immune response.

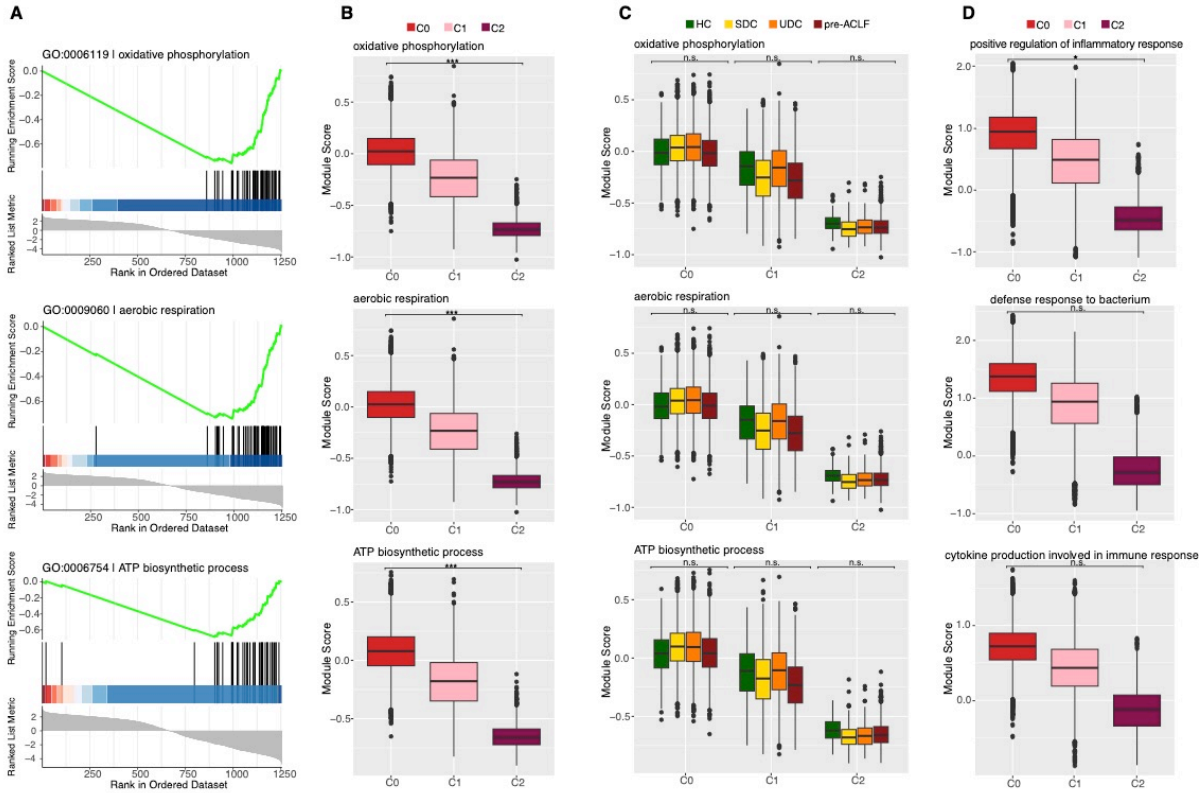

Figure 4. GSEA of key biological processes defining monocyte subpopulations.
(A) GSEA results for the three biological processes: oxidative phosphorylation, aerobic respiration, and ATP biosynthetic process. Running Enrichment Score (green line) depicts the cumulative enrichment score as genes are ranked by expression level. Ranked List Metric (bottom grey plot) shows the correlation of genes with the phenotype of interest across the ranked dataset. The heatmap (middle colored bar) represents the distribution of gene ranks—with red for positive correlation, blue for negative correlation, and white for a midpoint. **(B)** Boxplots showing the mean pathway signature score for the three processes for each monocyte subset and **(C)** for each group. Differences in module scores were assessed using Kruskal Wallis Test.***adjusted *p*-value <0.001; n.s. not significant**. (D)** Average gene expression trends across monocytic subsets related to Positive regulation of inflammatory response, Defense response to bacterium, and Cytokine production involved in immune response. Asterisks indicate reaching a significant nominal *p*-value, whereas the adjusted *p*-value was not significant. Differences in module scores were assessed using Kruskal Wallis Test. *nominal *p*-value <0.05. *Abbreviations:* HC, healthy controls; n.s., not significant; pre-ACLF, pre-acute-on-chronic liver failure; SDC, stable decompensated cirrhosis; UDC, unstable decompensated cirrhosis.

Identification and translation of a C2 monocytic gene signature to whole blood profiles

Given the identification of a specific population of C2 monocytes expanded in pre-ACLF patients by CITE-seq of the PBMCs and the availability of transcriptional data from the whole blood of the same patients (**Figure 1 B**), we aimed to investigate whether a C2-associated gene signature could still be detected in whole blood in the included patients. First, based on scRNA-seq data, we selected genes to define such a signature by combining three criteria: (i) they were upregulated in classical monocytes when compared with the rest of the cell types; (ii) they were upregulated when comparing C2 with the other subtypes of classical monocytes; and (iii) they were upregulated within C2 when comparing pre-ACLF and healthy controls/SDC/UDC. As a result, we identified 96 upregulated genes that characterize the C2 monocytes subset in pre-ACLF patients (**Figure 5 A**).

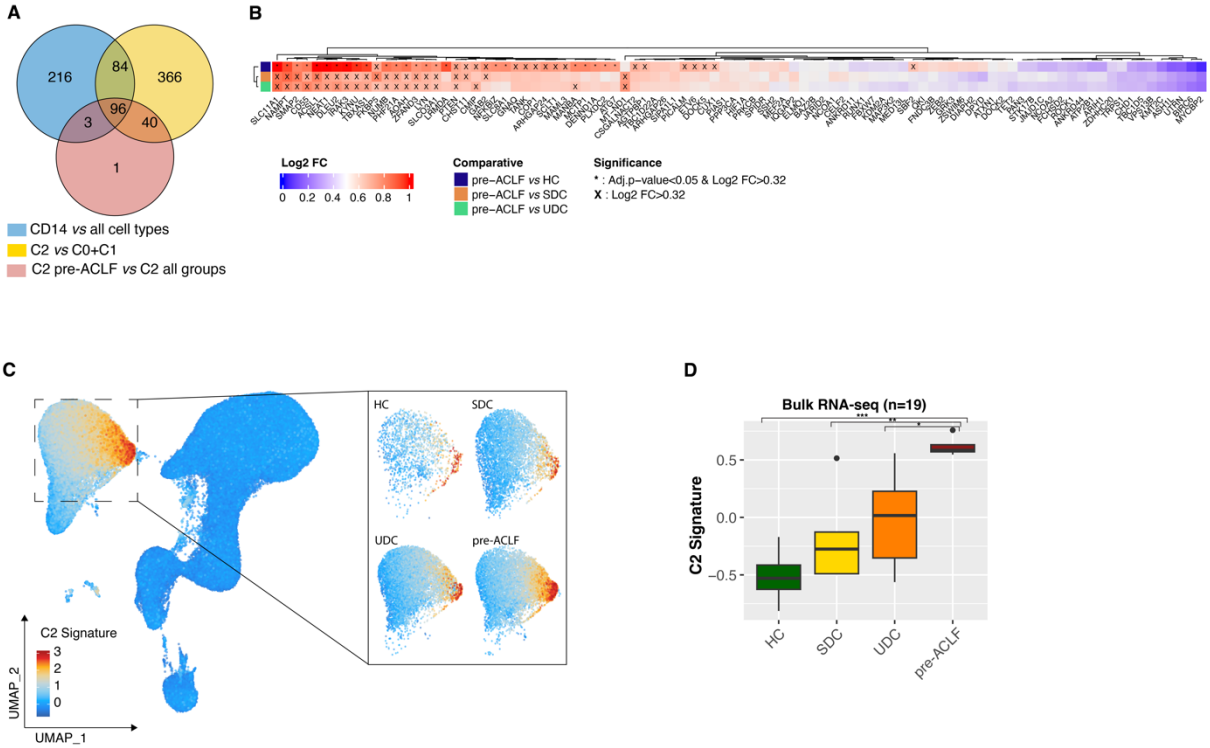

Figure 5. Identification of the C2 signature in whole blood RNA-seq data.
(A) Venn diagram illustrates the overlap of DEGs at single-cell resolution among three comparisons: classical monocytes versus all other cell types (blue), C2 versus Clusters 0 and 1 (yellow), and C2 pre-ACLF versus C2 in all groups (HC, SDC, and UDC (red). **(B)** Heatmap showing the scaled log2 FC levels of the selected DEGs from different comparatives in bulk RNA-seq: HC/SDC/ UDC vs. pre-ACLF. The color scale represents the log2 fold-change, with blue indicating downregulation and red indicating upregulation. Significant DEGs with log2 FC > 0.32 and adjusted p-value < 0.05 are marked with an asterisk; genes with a tendency (log2 FC > 0.32) are marked with a cross. **(C)** UMAP shows the distribution of the expression of the C2 signature. The inset panels show the distribution of C2 signature across different groups. **(D)** Boxplot displaying the module score for the C2 signature across the paired bulk RNA-seq data, categorized by group. *Abbreviations:* HC, healthy controls; Log2FC, logarithmic 2 Fold Change; pre-ACLF, pre-acute-on-chronic liver failure; SDC, stable decompensated cirrhosis; UDC, unstable decompensated cirrhosis.

335 Next, we analyzed the expression profiles of these 96 genes in whole blood, with 94 genes being
336 expressed at the bulk level. Then, we selected those genes with a fold change higher than 25% in bulk
337 RNA-seq, equivalent to log2 FC> 0.32, for the three comparisons: healthy controls/SDC/UDC vs. pre-
338 ACLF. As a result, we identified 18 genes defining the C2-signature at whole blood level: *SLC11A1*,
339 *NAMPT*, *SMAP2*, *CD55*, *ACSL1*, *NEAT1*, *DLEU2*, *IRAK3*, *KYNU*, *TBXAS1*, *FKBP5*, *NUMB*, *PHF21A*, *AOAH*,
340 *ZFAND3*, *LYN*, *SLCO3A1*, and *PTEN* (**Figure 5 B**).

341 Subsequently, we computed an activity score associated with the defined C2 signature to assess its
342 profile in both single-cell PBMC and whole-blood RNA-seq data (**Figure 5 C, D**). We computed such
343 activity value using a signature score (see Material and Methods: Module scores), in which higher
344 values indicate high activity of the gene sets in each sample or cell. As expected, we observed a
345 significant progressive increase in the C2 signature activity score from healthy controls to SDC and
346 UDC, culminating in the pre-ACLF group, which showed the highest levels at both the single-cell
347 (PBMCs) (**Figure 5 C**) and bulk (whole blood) levels (**Figure 5 D**).

348 These findings highlight the efficient translation of the C2 monocytic signature from the cellular to the
349 systemic level and its enrichment in pre-ACLF patients.

350 ***Validation of C2 gene signature in two prospective multicenter cohorts of patients with AD***

351 To validate the clinical significance of the defined C2 gene signature, we evaluated its relevance in two
352 large and independent prospective multicenter cohorts of patients with AD from Europe (PREDICT;
353 n=689) and from Latin America (ACLARA; n=521) (**Figure 6 A**). In both cohorts, whole blood samples
354 were collected at hospital admission, and bulk RNA-seq was performed. In PREDICT, patients were
355 followed up for 90 days and classified as SDC, UDC or pre-ACLF based on their clinical trajectory
356 (**Supplementary Figure 9, Supplementary Table 5**). In the ACLARA cohort, patients were followed up
357 for 28 days and classified as either AD or pre-ACLF (**Supplementary Figure 10, Supplementary Table**
358 **6)**. Detailed description of patient selection from both cohorts are provided in the Material and
359 Methods section and **Supplementary Figures 11 and 12**.

360 After computing the C2 signature activity score in both the PREDICT and ACLARA cohorts, we observed
361 a significant positive correlation with indicators of liver disease severity, including total bilirubin,
362 MELD, and CLIF-C AD score in patients from both cohorts at hospital admission (**Figure 6 B and**
363 **Supplementary Tables 7 and 8**). In line, it was significantly enriched in the pre-ACLF group as well as
364 in non-survivors in both cohorts (**Figure 6 C, D**), emphasizing the identified classical monocyte subtype
365 (C2) to be associated with disease severity, AD progression, and fatal outcome in patients with AD.

366 In the next step, we asked which pathophysiological processes might primarily be associated with an
367 increased expression of the C2 gene signature in patients with AD. We performed additional
368 correlation analysis between the C2 gene signature score and clinical and laboratory parameters of
369 AD patients from both cohorts at hospital admission. We found a significant positive correlation of the
370 C2 score with white blood cell count and C-reactive protein in both cohorts (**Supplementary Figure 13**
371 **A and Supplementary Tables 7 and 8**). Moreover, upon dividing the cohorts into patients with and
372 without bacterial infection, we observed additionally higher C2 signature activity scores in patients
373 with bacterial infection compared to those without infection in patients from the SDC and UDC groups
374 of the PREDICT cohort (**Supplementary Figure 13 B**).

The C2 signature activity score had an AUROC for ACLF or death in both PREDICT and ACLARA cohorts around 0.65 (**Figure 6 E)**. However, combining the newly identified C2 signature score with the CLIF-C AD score did not significantly improve the latter´s predictive capability regarding outcomes of ACLF and death (**Supplementary Figure 14**).

In summary, we demonstrated that the C2 signature can be detected in whole blood RNA-seq data from AD patients and, crucially, is associated with bacterial infection, progression to ACLF and mortality in two independent cohorts.

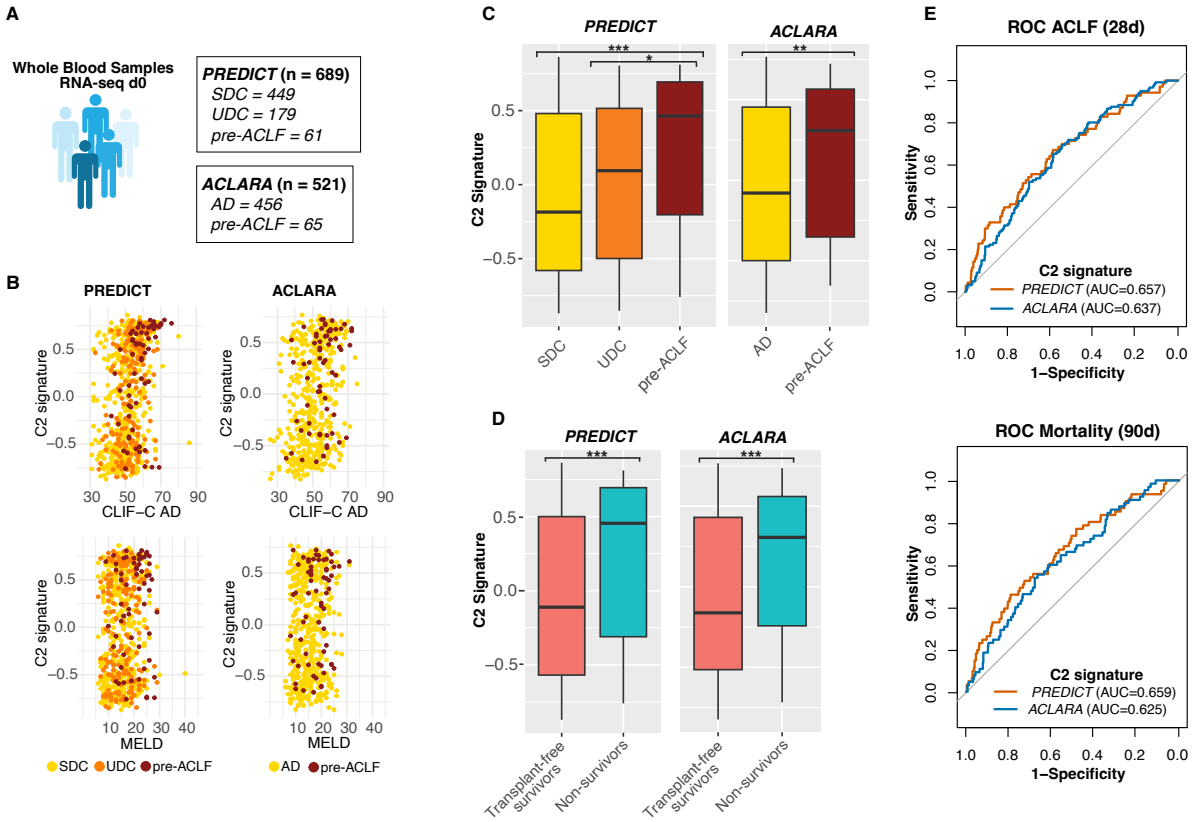

Figure 6. C2 monocytic subcluster validation in two independent AD cohorts.
(A) C2 signature was assessed in whole blood RNA-seq data collected at day 0 (d0) from two independent cohorts of AD patients. PREDICT cohort (top) accounted for data from 689 patients who were labeled 90 days after HA as SDC (n=449), UDC (n=179), or pre-ACLF (n=61). ACLARA (bottom) accounted for data from 521 patients who were labeled 28 days after HA as AD (n=456) or as pre-ACLF (n=65). **(B)** Correlation analysis of C2 signature values with CLIF-C AD and MELD across different patient groups in PREDICT (left) and ACLARA (right) cohorts. Top row: C2 signature vs. CLIF-C AD count. Bottom row: C2 signature vs. MELD levels. Each point represents an individual, colored by patient group: SDC, yellow; UDC, orange; pre-ACLF, dark red for the PREDICT cohort, and AD, yellow and pre-ACLF, dark red for the ACLARA cohort. **(C)** Boxplots display the average expression of the C2 signature among the different groups in PREDICT (left) and ACLARA (right) cohorts. Wilcoxon Signed-Rank Test was used to assess the differences between groups. **(D)** Boxplots display the average expression of the C2 signature between patients that died (pink) vs. patients that did not die (turquoise) in PREDICT (left) and ACLARA (right) cohorts. Wilcoxon Signed-Rank Test was used to assess the differences between groups**. (E)** ROC curves showing the predictive capacity of the C2 signature regarding outcomes ACLF (top) and mortality (bottom) for the PREDICT (red) and the ACLARA (blue) cohorts. *** Adjusted *p*-value < 0.001; ** Adjusted *p*-value < 0.01; * Adjusted *p*-value < 0.05. *Abbreviations:* AD, acute decompensation; AUC, area under the curve; d0, day 0; HC, healthy controls; PBMCs, peripheral blood mononuclear cells; pre-ACLF, pre-acute-on-chronic liver failure; ROC, Receiver-operating characteristic curve; SDC, stable decompensated cirrhosis; UDC, unstable decompensated cirrhosis.

402 ***Validation of impaired energy metabolism in AD patients progressing to ACLF***

403 To further validate the relevance of impaired energy metabolism in AD patients progressing to ACLF,
404 we conducted respirometry analyses in an additional prospective, single-center cohort of 12 AD
405 patients (**Supplementary Table 14**). Patient recruitment took place at the center in Aachen, Germany,
406 between 2021 and 2024 and inclusion/exclusion criteria were identical to those applied for the single-
407 cell study cohort (Supplementary Table 9). After 90 days of follow-up, 8 patients were classified as SDC
408 or UDC, and 4 as pre-ACLF (ACLF development within 28 days). Whole blood samples were collected
409 at hospital admission, and classical monocytes were subsequently isolated. Mitochondrial function
410 was assessed using Respirometry in Frozen Samples (RIFS) on a Seahorse Extracellular Flux Analyzer
411 (Agilent), targeting the entire classical monocytes population.

412 Notably, despite analyzing the total CD14+ monocyte pool, we observed a progressive decline of the
413 Complex IV activity, measured by oxygen consumption rate (OCR), in pre-ACLF patients compared to
414 SDC and UDC (**Figure 7 C**). In contrast, no significant differences were detected in the maximal
415 respiratory capacity driven through Complex I or II (**Figure 7 A, B**). Notably, this decline in Complex IV
416 function mirrors transcriptional downregulation seen specifically in the C2 subset, which constitutes
417 only a fraction of the classical monocyte population. The persistence of this signal at the whole-
418 population level highlights the biological relevance of our findings and supports a model in which
419 monocyte metabolic dysfunction contributes to AD progression and the development of ACLF.

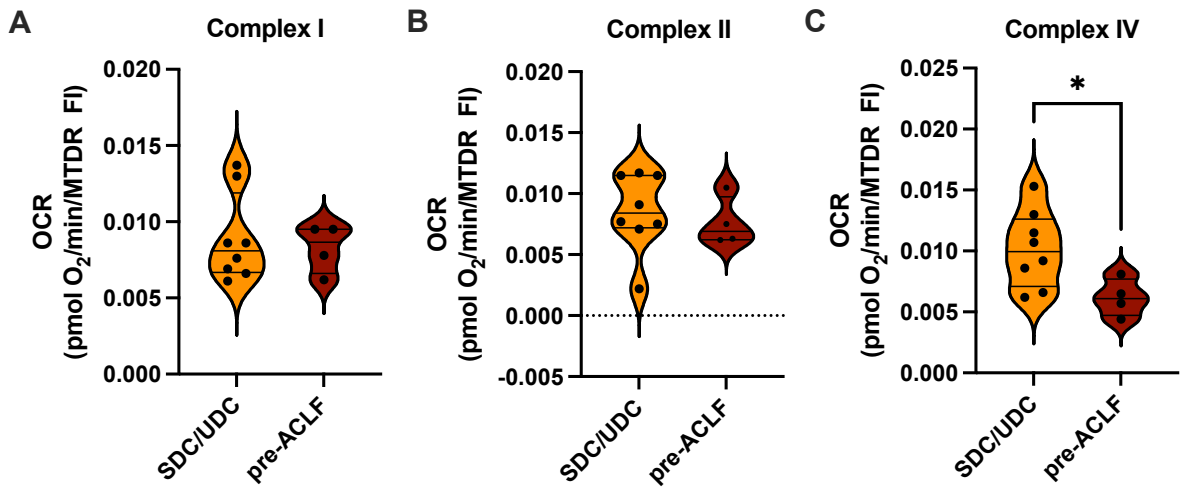

420

421 ***Figure 7. Validation of impaired monocytic mitochondrial function in an additional cohort of AD patients.***
422 Violin plots displaying the oxygen consumption rate (OCR) driven by respiratory chain complexes I, II and IV **(A-**
423 **C)** respectively, as assessed by respirometry analysis using Seahorse Extracellular Flux Analyzer. Each subfigure
424 compares SDC/UDC patients with AD patients with ACLF development within 28 days ("pre-ACLF").
425 Measurements were applied to the entire population of CD14+ monocytes, with each point representing the
426 average of duplicate measurements from one patient. An unpaired t-test was used to assess statistical
427 differences between the groups, * *p*-value < 0.05. *Abbreviations:* MTDR FI, MitoTracker Deep Red Fluorescence
428 Intensity; OCR, oxygen consumption rate; pre-ACLF, pre-acute-on-chronic liver failure; SDC, unstable
429 decompensated cirrhosis; UDC, unstable decompensated cirrhosis.

430 # Discussion

431 This European multicenter study prospectively investigated transcriptomic alterations of peripheral
432 immune cells at single-cell resolution in patients with AD. We found that classical monocytes showed
433 the most pronounced transcriptional regulation among the investigated immune cells. A monocytic
434 subpopulation, termed C2, was identified correlating with the onset of ACLF. This subpopulation was
435 characterized by impaired cellular energy supply. Notably, the transcriptomic signature of these cells
436 remained significantly associated with bacterial infection, ACLF development, and mortality in whole-
437 blood bulk RNA-seq data of two large prospective multicenter cohorts of patients with AD.

438 While previous studies on ACLF had a case-control design, making it impossible to determine whether
439 the observed changes were preceded or were the consequence of ACLF (18–20), our prospective
440 study analyzed changes in peripheral immune cells in patients with AD *before* development of ACLF.
441 Classical monocytes were identified to show the highest transcriptional regulation of all investigated
442 immune cells during AD. Various studies have consistently reported an overrepresentation of
443 monocytic gene signatures among regulated genes in the blood of patients with manifest ACLF (17,18).
444 Our analysis revealed that those significant transcriptional alterations identified in classical
445 monocytes, in fact, can be observed much earlier in the disease course, even in the early stages of AD.
446 These findings indicate monocytes to play a pivotal role in AD and support their involvement in disease
447 progression.

448 In-depth exploration of classical monocytes identified three major subclusters: C0, C1, and C2. The C2
449 subcluster showed an expanded presence in pre-ACLF patients (up to 10%) and correlated with latency
450 towards ACLF. C1 appeared as an intermediate state, illustrating the progressive alterations in
451 monocyte populations as cirrhosis advances. Consequently, we focused our analysis on the differences
452 between the C0 and C2 subclusters. Interestingly, the C2 subset was not only detectable in patients
453 with pre-ACLF but – to a lesser extent – already in healthy controls and patients from the other AD
454 groups. This suggests that the C2 monocytic subpopulation already exists in physiological conditions
455 and expands as the disease progresses.

456 In 2018, Bernsmeier et al. described an expansion of mononuclear myeloid-derived suppressor cells
457 (M-MDSCs, $CD14^{+}HLADR^{lo/-}CD15^{-}$) in ACLF patients associated with impaired antimicrobial response
458 (23). We questioned whether our newly identified C2 subcluster shares features with M-MDSCs. While
459 the expression of *CD14, HLA-DR, CD163, CX3CR1,* and *CCR5* was decreased and pointed in the same
460 direction, the expression of *CD15, MERTK*, and *CD86* was increased, in contrast to the M-MDSC
461 phenotype. Furthermore, the expression of *S100A8* and *S100A9*, which encode for two pro-
462 inflammatory mediators preferentially secreted by M-MDSCs (23), were downregulated in the C2
463 subset. Thus, we propose that the C2 monocyte subpopulation represents a previously undescribed
464 monocyte subset associated with AD progression.

465 To further characterize the C2 subpopulation, transcriptomic profiling was conducted using marker
466 genes of monocyte differentiation and expansion during cirrhosis progression. Various genes encoding
467 proteins related to inflammatory and immune responses, including interleukin-1 receptor-associated
468 kinase 3 (*IRAK3*), hypoxia-inducible factor 1α (*HIF-1α*), and toll-like receptor 2 (*TLR2*), were
469 upregulated in the C2 subset. In contrast, genes linked to *suppressed* immune responses were
470 increasingly expressed, including *MERTK*, which is associated with immunoregulatory monocytes in

471 patients with ACLF (24) and *VCAN*, encoding versican, which was found to be associated with an
472 immunosuppressive phenotype of monocytes in sepsis (25). Conversely, genes encoding pro-
473 inflammatory S100 proteins (*S100A8, S100A9, S100A12)*, and key genes relevant to bacterial immune
474 response, such as *CD68* and *LYZ*, were downregulated in the C2 subset. These findings suggest that C2
475 monocytes exhibit early signs of immunological dysfunction, potentially increasing susceptibility to
476 bacterial infections, as key precipitant of ACLF. Our hypothesis was validated in whole blood bulk RNA-
477 seq data from two large and independent cohorts, including more than 1200 AD patients (PREDICT
478 and ACLARA). Here, the C2 signature not only positively correlated with liver disease severity but was
479 even more evident in AD patients with simultaneous bacterial infections. These findings highlight the
480 importance of the C2 signature not only in cirrhosis progression but also in precipitating events that
481 lead to ACLF.

482 The immunoregulatory features of C2 monocytes raised the possibility that this subset might resemble
483 endotoxin-tolerant monocytes, as previously observed in cirrhosis patients (25). However, comparison
484 of the transcriptomic profile of C2 monocytes with a well-established dataset of sepsis-associated
485 monocytes revealed only limited overlap. These findings argue against a primarily endotoxin-tolerant
486 identity and instead suggest that C2 represents a functionally distinct monocyte population in the
487 context of AD and ACLF progression.

488 To gain deeper insight into the biological function of C2 monocytes during cirrhosis progression,
489 pathway analysis was performed. Although our analysis revealed a clear trend of reduced immune
490 function within the C2 subset, immune-related pathways were not significantly altered. Instead, our
491 analysis revealed a dominant downregulation of genes that encode key enzymes in cellular energy
492 supply. To functionally validate these findings, Seahorse respirometry was conducted in an
493 independent cohort of 12 AD patients, assessing mitochondrial function in the entire classical
494 monocyte population. Despite analyzing all CD14+ monocytes, a progressive decline in Complex IV-
495 dependent OCR was observed in pre-ACLF patients. These results are consistent with our gene
496 expression data, which revealed a specific downregulation of Complex IV encoding genes within the
497 C2 subset. The fact that this metabolic dysfunction was detectable across the entire monocyte
498 population underscores its potential relevance for AD progression.

499 A reduction in cellular energy supply, particularly in ATP production, was reported to impair essential
500 immune functions such as phagocytosis, cytokine production, and antigen presentation, and to
501 worsen clinical outcome e.g. in patients with sepsis (27). We hypothesize, that in patients with AD,
502 these dysfunctions could limit the capacity of monocytes to respond effectively to infections and
503 increase susceptibility to infections, a critical concern in the context ACLF development.

504 Our results not only strengthen the hypothesis that bioenergetic failure in monocytes is a key
505 contributor to ACLF development. They also align with prior studies reporting a progressive metabolic
506 dysfunction in patients with cirrhosis, AD, and ACLF, likely driven by systemic inflammation (19,28–
507 31). Importantly, the identification of a specific monocytic subset that is predominantly characterized
508 by bioenergetic failure and early immune exhaustion, reinforces the hypothesis of systemic
509 inflammation-associated energetic exhaustion during cirrhosis progression, preceding ACLF
510 development (32,33). Systemic inflammation in cirrhosis is partly driven by bacterial translocation,
511 and current therapeutic strategies aim to modulate gut barrier function and microbiota diversity,
512 using interventions such as rifaximin or fecal microbiota transfer (34,35). The identification of a

513 monocytic subset that is characterized by bioenergetic failure and expands before ACLF onset provides
514 additional rationale for interventions targeting inflammation-induced metabolic exhaustion in
515 patients with AD. Moreover, this subset could serve as a model to develop and test therapeutic
516 strategies aimed at restoring immune cell function and preventing ACLF progression.

517 Despite the valuable insights gained from this study, complementary omics or functional assays are
518 needed to further mechanistically validate our findings and pinpoint potential intervention targets.
519 Moreover, longitudinal single-cell analyses would be beneficial to elucidate the dynamic changes in
520 monocyte subsets throughout disease progression.

521 In summary, our analysis provides strong evidence that monocytes, particularly a novel subset termed
522 C2, play a critical role in cirrhosis progression and the development of ACLF. We show that C2
523 monocytes exhibit a transcriptional profile indicative of immuno-metabolic exhaustion, which may
524 increase susceptibility to bacterial infections. These findings highlight the therapeutic potential of
525 targeting bioenergetic failure in immune cells as a strategy to intervene cirrhosis progression.

Material and Methods

Study design

A prospective multicenter study was conducted in 5 European centers (Hôpital Beaujon, Université Paris-Cité, France; Goethe University Frankfurt, Germany; RWTH Aachen University, Germany; University of Bologna, Italy; University of Turin, Italy) between October 2020 and July 2021. Patients who were admitted to the hospital due to AD (ascites, overt hepatic encephalopathy, new onset of non-obstructive jaundice, gastrointestinal hemorrhage, and/or bacterial infections) met the inclusion criterion and were screened for exclusion criteria (**Supplementary Table 9**). A total of 63 patients with AD and 15 healthy controls were recruited. Written informed consent was obtained from the patient, her/his spouse, or the appointed legal guardian upon hospital admission. Clinical data were collected, and sample acquisition was performed within 72 hours after hospital admission in all included patients. Patients were followed up for 90 days, and readmission due to AD, development of ACLF, and outcome were documented (for detailed study design and visit schedule, **Supplementary Figure 1** and **Supplementary Table 10**). The study protocol was approved by the local ethics committee of each participating center (Paris, Frankfurt, Aachen, Bologna, Turin) and conducted in accordance with the Declaration of Helsinki.

Sample collection and PBMC isolation

After study inclusion, peripheral blood was drawn from all participants from the single-cell study cohort, using BD vacutainer CPT tubes (BD Biosciences; (36)) for PBMC isolation and TempusTM tubes (Applied Biosystems) for whole blood assessment. After density gradient centrifugation at 1500 RCF for 20 minutes at 20°C PBMCs were aspirated and then cryopreserved using fetal calf serum with 10% DMSO. The cells were gradually frozen and stored at -80°C for several weeks until library preparation and sequencing or flow cytometry analysis, respectively.

Group allocation and patient selection strategy for single-cell analysis

90 days after study inclusion, patients were classified according to their clinical course as no readmission due to AD ("stable decompensated cirrhosis", SDC, n=46), readmission due to AD ("unstable decompensated cirrhosis", UDC, n=8) or ACLF development within 28 days ("pre-ACLF", n=10). The diagnostic criteria of ACLF were according to the EF-CLIF definition (5). Of the 63 recruited patients, samples from 4 pre-ACLF, 6 UDC, and 6 SDC patients, along with four healthy controls, were selected to represent the entire study cohort and subjected to CITE-seq profiling (detailed in **Supplementary Material** and **Supplementary Tables 1,2,3**). For baseline characteristics analysis, categorical variables were summarized as counts (percentages), and continuous variables as median (interquartile range, IQR). The Wilcoxon–Mann–Whitney test was used for continuous variables, and the chi-square test for categorical variables.

CITE-seq

Library preparation, sequencing, and demultiplexing

The isolated PBMCs were recovered by gently thawing and immediately diluting in pure FCS. Next, cells were centrifuged at 500 RCF for 7 minutes at 20°C, and the supernatant was removed. PBMCs were then resuspended in 4 ml 5% FCS in PBS and filtered through a 20 µm pluriStrainer® provided by pluriSelect (Leipzig, Germany) to obtain a single-cell solution. After the PBMCs were passed through a

567 strainer, a second centrifugation was performed. The supernatant was removed, and cells were
568 diluted in 100 µl 5% FCS in PBS. 5 µl Human TruStain FcX (BioLegend) was added and incubated for 10
569 minutes at 4°C.

570 A panel of 23 TotalSeq-C antibodies (BioLegend) was pooled, using 0.5 µg of each antibody
571 (**Supplementary Table 11**). Samples were incubated with the TotalSeq-C antibody pool for 30 min at
572 4°C. Cells were washed two times using 3 ml 5% FCS in PBS and rediluted in 1.5 ml of sorting buffer
573 (5% FCS in PBS).

574 For the detection of dead cells, DAPI was added at a final concentration of 0.5 µg/ml. Up to 300,000
575 cells from each sample were sorted on a Sony Cell Sorter by life/dead sorting. Sorted viable cells were
576 resuspended in 10 µl 1% BSA in PBS, counted, and ~20,000 cells in 38.7 µl were applied to single cell
577 partitioning and barcoding *via* Chromium Controller (10x Genomics).

578 Each participant's sample was prepared into two distinct libraries: (I) 5' Gene Expression Library (GEX),
579 designed for scRNA-seq to capture transcriptome data; and (II) Surface Protein Library, which utilized
580 TotalSeq-C barcodes to profile surface proteins, aligning with the CITE-seq methodology.

581 Cell Ranger (v6.01) was used for read alignment, filtering, barcode processing, and UMI counting with
582 default settings (37). GRCh38-2020 was used as the transcriptome reference. Specifically, STAR was
583 used in FASTQs alignment (38). Cell barcodes were then automatically determined based on the
584 distribution of the UMI count.

585 *Pre-processing*

586 We used the R package *Seurat* v4.3.0 (39) to preprocess the gene-barcode matrix and the surface
587 protein matrix of both patients and healthy controls and to perform further analysis. For each sample,
588 genes not observed in at least three cells were dropped. Low-quality or damaged cells were excluded
589 using a combination of a number of expressed genes (cells with <300 and >3500 genes) and
590 mitochondrial transcript percentages (cells with >10% mitochondrial genes). Each sample dataset was
591 normalized using the *'SCTransform'* function (40) from the *Seurat* package and regression of
592 mitochondrial RNA and cell cycle genes.

593 *Integration, clustering, and cell type identification*

594 The filtered and cleaned single-cell dataset underwent a process to identify highly variable genes and
595 remove unwanted sources of variation. This was done by calculating and extracting a subset of
596 features that show high cell-to-cell variation in the dataset using the '*FindVariableFeatures'* Seurat's
597 function. Additionally, the *'FeatureScatter'* plot from *Seurat* was applied, and we removed the
598 detected outliers when plotting feature-feature relationships (41). Harmony was used to correct for
599 batch effects (42). For each sample where the protein surface markers data was available, we selected
600 the most variable protein sub-space and applied feature-wise centered log-ratio transformation (CLR)
601 (43). Data were visualized using UMAP. Data were scaled, and the dimensionality was reduced by PCA.
602 To identify cell clusters, a shared nearest neighbor (SNN) graph was built using distances in PCA space
603 (top 1 to 20 components) through Seurat's *'FindNeighbors'* function. The Louvain algorithm was then
604 employed to iteratively cluster neighboring cells using Seurat's *'FindClusters'* function, using a
605 resolution parameter of 0.5. Cell type annotation was done by combining three parallel evaluations:
606 gene expression of canonical marker genes (**Supplementary Figure 2**), surface protein markers

607 (**Supplementary Figure 3 A, B**), and Azimuth results (a reference-based approach using an external
608 well-annotated dataset of PBMCs (39)).

609 *Cluster Composition Analysis: changes in cell proportions between groups*

610 Differences in cell type proportion between conditions were assessed by comparing the proportional
611 differences in cell populations between AD patients and healthy controls for both gene expression and
612 protein surface markers data, utilizing the *'sc_utils'* function from *scProportionTest* package with
613 default parameters (44). The estimations of the p-value and the confidence interval of the magnitude
614 of the difference are computed respectively using a permutation test and bootstrapping.

615 *Differential expression analysis, pathway analysis, and trajectory analysis*

616 Seurat *'FindAllMarkers'* function with the default Wilcoxon rank sum test based on the normalized
617 data was used to identify the cluster markers used for cluster annotation. The '*FindMarkers'* function
618 was employed to identify markers for each cell cluster to measure differential gene expression
619 between conditions, using the default Wilcoxon rank sum test method. Genes detected in less than
620 50% of both evaluated groups were discarded. We considered differentially expressed genes (DEG) to
621 be statistically significant if the adjusted p-value < 0.05 (Benjamini-Hochberg (BH)) and absolute Fold
622 Change (FC) > 1.5. '*VlnPlot*', '*FeaturePlot*,' and '*Dotplot'* functions were applied to visualize gene
623 expression in each cell type or group.

624 Next, Gene Set Enrichment Analysis (GSEA) was performed using the R package *ClusterProfiler* (45),
625 considering the comprehensive functions included in Gene Ontology (GO). Biological pathways in
626 which genes appeared at a different frequency than expected were considered enriched. The results
627 were visualized using default enrichment plots. Enrichment scores with p-value adjusted < 0.05 were
628 considered significant. The differences in the pathways among patient groups were computed using
629 the non-parametric Kruskal Wallis test.

630 Single-cell trajectory analyses were computed using the *'learn_graph'* function from the *Monocle3*
631 package with default parameters (46). We then plot the cells based on their *pseudotime*.

632 *Module scores for specific gene sets*

633 We utilized cell module scores to quantify the extent of individual cell expression of specific
634 predefined gene sets. For this purpose, we used the '*AddModuleScore'* function from *Seurat* with
635 default settings. The lists of genes defining this module were prepared based on the intersection of
636 upregulated DEGs resulting from various differential expression analyses (DEA). Differences in module
637 scores were assessed using the non-parametric Kruskal Wallis test.

638 Bulk RNA-seq

639 *Library preparation, sequencing and demultiplexing*

640 Bulk RNA-seq was performed in collaboration with the Genomics platform of the Center for
641 Cooperative Research in Biosciences (CIC bioGUNE), Derio, Bizkaia, Spain. RNA was extracted from
642 whole blood collected in Tempus™ tubes from the single-cell study cohort using the Extraction
643 Tempus™ Spin RNA Isolation Kit (Applied Biosystems). The extracted RNA was treated with DNase.
644 RNA quality was assessed using Agilent RNA 6000 Nano and Pico Chips (Agilent Technologies). RNA
645 concentration was assessed using RNA HS Assay Kit in a Qubit 2.0 fluorometer (Thermo Fisher
646 Scientific).

647 Sequencing libraries were prepared using the NuGEN UniversalPlus mRNA-Seq with NuQuant kit
648 (Tecan Life Sciences, Cat.#0520-24) and following the user guide (M01485v6.1andv7). The kit is
649 intended to prepare sequencing libraries depleted of globin. Briefly, starting from 500 ng of total RNA,
650 rRNA, and globin mRNA were depleted, and the remaining RNA was purified, fragmented, and primed
651 for cDNA synthesis. cDNA first strand was synthesized with SuperScript-II Reverse Transcriptase
652 (Thermo Fisher Scientific, Cat.#18064-014) for 10 min at 25°C, 15 min at 42°C, 15 min at 70°C and
653 pause at 4°C. The second strand of cDNA was synthesized with Illumina reagents at 16°C for 1 hour.
654 Then, A-tailing and adaptor ligation were performed. Finally, enrichment of libraries was achieved by
655 PCR (30 s at 98°C; 15 cycles of 10 s at 98°C, 30 s at 60°C, 30 s at 72°C; 5min at 72°C and pause at 4°C).

656 Afterward, libraries were visualized on an Agilent 2100 Bioanalyzer using Agilent High Sensitivity DNA
657 kit (Agilent Technologies, Cat. # 5067-4626), quantified using Qubit dsDNA HS DNA Kit (Thermo Fisher
658 Scientific, Cat. # Q32854) and sequenced in a NovaSeq-6000 (Illumina Inc.) by at least 40 million
659 paired-end 100nt reads.

660 Raw reads were demultiplexed via bclfastq2 Conversion Software v2.20 (Illumina) to convert base call
661 (BCL) files into FastQ files. Quality control of FastQ files was performed using FastQC (Bioinformatics
662 Babraham Institute) (47), and reads were trimmed for contaminating sequence adapters and poor-
663 quality bases using Trimmomatic (48). Sequencing reads were aligned to the Human (GRCh38) genome
664 with STAR (2.6.1) setting the parameters to default values (38). Uniquely aligned reads were assigned
665 to GENCODE18 gene annotations using HTSeq v0.11 and quantified with htseq-counts run in stranded
666 mode with default parameters (49).

667 *Bulk RNA-seq downstream analysis*

668 R v4.3.0 was employed in the downstream analysis of RNA-seq data. Genes exhibiting more than 1
669 count per million (CPM) in at least three samples were selected for the analysis. Utilizing the *limma-*
670 *voom* workflow (50), RNA-seq count data was normalized, and variance estimation was performed.
671 PCA was applied to the normalized data to assess sample similarity.

672 *Module scores*

673 A module score was calculated for each evaluated sample group using the Gene Set Variation Analysis
674 (*GSVA*) R package v1.42.0 (51) in the single-cell paired bulk RNA-seq, as well as in the PREDICT and the
675 ACLARA cohorts. This gene signature was calculated using previously selected genes to compute the
676 module score at the single-cell level.

677 Flow Cytometry Analysis

678 Flow cytometry of peripheral $CD14^+$ monocytes was conducted. For this purpose, additional PBMC
679 aliquots from the single-cell study cohort were used. First, PBMCs were thawed gently, as described
680 above. Subsequently, $CD14^+$ cells were enriched by magnetic cell separation using positive selection
681 for human CD14 (Miltenyi Biotec, Bergisch Gladbach, Germany) for in vitro experiments.

682 For surface marker expression analysis, $CD14^+$ peripheral monocytes were incubated with
683 fluorochrome-conjugated primary antibodies at optimal dilutions at 4°C for 30 min in PBS containing
684 0.5% fetal calf serum and 2 mmol/L EDTA. Single-color staining, isotype-matched controls (IMCs), and
685 fluorescence minus one (FMO) controls were applied. The antibodies used were CD14 (clone HCD14),
686 CD16 (3G8), and human leukocyte antigen-DR (HLA-DR) (G46-6).

687 Cell viability was determined with the LIVE/DEAD™ Fixable Aqua Dead Cell Stain Kit from Thermo
688 Fisher and IMC mouse IgG1 κ and IgG2a κ isotype controls from BD Pharmingen (BD Biosciences,
689 Franklin Lakes, NJ, USA). Flow cytometry analysis was performed using a FACS Canto II flow cytometer
690 and FlowJo (v10) software (BD Biosciences, Franklin Lakes, NJ, USA). Delta mean fluorescence intensity
691 (ΔMFI) was calculated by subtracting the mean MFI count in the SDC group from single MFI counts in
692 the four study groups. The Wilcoxon–Mann–Whitney test was used to test statistical differences
693 within the four study groups.

694 *Validation cohorts*

695 *Validation studies* were conducted using whole blood bulk RNA-seq data from two prospective,
696 multicenter European and Latin America cohorts, PREDICT and ACLARA (7,52). The inclusion and
697 exclusion criteria of both cohorts are shown in **Supplementary Tables 12 and 13**. Both cohorts
698 collected various measures, including clinical, pharmacological, and outcome data from AD patients
699 upon hospital admission and during follow-up visits (**Supplementary Tables 5 and 6**). The follow-up
700 period was 90 days for PREDICT and 28 days for ACLARA (**Supplementary Figures 7 and 8**). 90 days
701 after study inclusion, AD patients from the *PREDICT* cohort were categorized into SDC/UDC and pre-
702 ACLF (7). *ACLARA* patients were classified either into AD or pre-ACLF. The diagnostic criteria of ACLF
703 in both cohorts were according to the EF-CLIF definition (5).

704 The criteria for inclusion in our investigation were AD at hospital admission, availability of data on
705 short-term outcomes (liver transplant, ACLF development, or death), clinical data, treatment, and
706 availability of biological samples (buffy coat, tempus, serum, and plasma). Based on these criteria, 768
707 AD patients from PREDICT were chosen for analysis, with 738 samples passing quality control after
708 sequencing. According to the definition of ACLF within the single-cell study cohort, only patients who
709 developed ACLF within 28 days after hospital admission were included (n=61, **Supplementary Figure**
710 **9**). For the ACLARA cohort, the same criteria applied, with the added requirement that samples be
711 available at the Barcelona EFCLIF biobank by the end of March 2021 due to COVID-19-related delays
712 in shipping from South America. From ACLARA, 549 AD cirrhosis patients were selected, with 32
713 lacking buffy coat samples and 27 failing quality control after sequencing (**Supplementary Figure 10)**.
714 In total, 689 patients from PREDICT and 521 patients from ACLARA were included to validate the
715 single-cell results.

716 PREDICT & ACLARA bulk RNA-seq

717 Whole blood RNA-seq from 1,210 patients with AD included in the PREDICT (n=689) (7) and the
718 ACLARA (n=521)(52) studies were conducted according to the above-described bulk RNA-seq protocol.

719 A module score was calculated for each evaluated sample group, obtaining a gene signature score, as
720 described in Material and Methods: Module scores. Pearson (parametric) and Spearman (non-
721 parametric) correlation coefficients were computed to assess the relationships between the module
722 score and clinical variables. The Area Under the Receiver Operating Characteristic (AUC-ROC) curve
723 using the "*pROC"* R package (53) was utilized to evaluate the relationship between the module score
724 and outcomes (54). The comparison of ROC curves was performed using DeLong's Test. The analysis
725 of mean differences in the computed module scores among patient groups was assessed using the
726 ANOVA test when more than two groups were compared and the Wilcoxon Signed-Rank test
727 otherwise.

728
729 *Respirometry analysis*
730
731 *Validation cohort and classical monocyte isolation*
732 To validate the single-cell results, we analyzed an independent cohort of 12 patients who were
733 prospectively recruited to the University Hospital in Aachen, Germany, between 2021 and 20204 due
734 to AD (**Supplementary Table 14**). Inclusion/exclusion criteria, clinical data collection and whole blood
735 sample acquisition were applied or performed respectively following the same procedure as for the
736 single-cell study cohort (**Supplementary Table 9**). After 90 days follow-up, patients were classified as
737 SDC, UDC ("SDC/UDC", n=8) or pre-ACLF (n=4) with ACLF development within 28 days.
738 Peripheral blood was drawn from all participants using SARSTEDT S-Monovette K3 EDTA. Mononuclear
739 cells were isolated by density gradient centrifugation at 1500 RCF for 20 minutes at 20°C with
740 Lymphocyte-H separation media (Cedarlane, Burlington, Ontario, Canada). CD14+ cells were enriched
741 by magnetic cell separation using positive selection for human CD14 (Miltenyi Biotec, Bergisch
742 Gladbach, Germany) and subsequently cryopreserved using fetal calf serum with 10% DMSO. Cells
743 were gradually frozen and stored at -80°C for several weeks prior to respirometry analysis.
744
745 *Seahorse measurements and determination of cellular mitochondria content*
746 Respirometry analyses of classical monocyte samples was conducted according to the protocol for
747 respiration measurement in previously frozen samples ("RIFS" (55)). Briefly, cells were thawed and
748 washed in unsupplemented Mitochondrial Assay Solution (MAS; 70 mM Sucrose, 220 mM Mannitol,
749 5 mM KH_2PO_4, 5 mM $MgCl_2$, 1 mM EGTA, 2 mM HEPES; pH 7.2). Cell counts were determined and
750 adjusted to $12.5x10^6$/ml by resuspension in MAS. Next, cells underwent three freeze-thaw cycles with
751 liquid nitrogen before use.
752
753 For Seahorse assay, 20 µL of the cell lysate with 250,000 cells/well loaded onto XFe96 microplates on
754 the day of the assay. The samples were centrifuged at 2100×g for 10 min and stopped without a break.
755 In a next step, samples were brought to a final volume of 150 µL with MAS supplemented with 100
756 µg/mL cytochrome c and 10 µg/mL alamethicin. Injections resulted in a final concentration of either 2
757 µM rotenone and 5 mM succinate or 1 mM NADH from Port A, 2 µM antimycin A and rotenone from
758 Port B, 0.5 mM TMPD and 1 mM Asc from Port C, and 50 mM sodium azide from Port D.
759
760 OCR measurements included one baseline measurement before substrate injection (NADH or
761 succinate/rotenone), two measurements after maximal substrate-driven respiration, two
762 measurements post-antimycin A/rotenone injection, two measurements following TMPD/ascorbate
763 addition, and two measurements after Complex IV inhibition with sodium azide. All measurements
764 were performed in technical duplicates.
765
766 For normalization to mitochondria content, samples were stained with 500 nM MitoTracker Deep Red
767 (MTDR) in PBS for 5 min in a black 96-well plate. After centrifugation at 2,100 xg for 5 minutes, wells
768 were washed with PBS to remove the MTDR. Fluorescence intensity (FI) was measured from the
769 bottom of the plate in a Tecan Spark 10 M Multimode Plate Reader using an excitation wavelength of
770 633 nm and an emission wavelength of 678 nm. OCR values were normalized to MTDR FI. Statistical
771 differences between AD patients without (SDC/UDC) and with ACLF development (pre-ACLF) within
772 28 days were assessed using an unpaired t-test.

Statistical Methods

All analyses were performed in the R Computing Environment version 4.0.3 (56). Statistical methods are described in detail above in each subsection. In all statistical analyses, we considered *p*-value < 0.05 as statistically significant. In case an adjusted p-value for multiple testing is considered, it is described in the text.

Github

The analysis pipeline and figure generation code are available at https://github.com/TranslationalBioinformaticsUnit/C2_ACLF_2025

Acknowledgements: We thank all participating centres for their efforts in patient recruitment and fruitful collaboration. We thank the Genomics Facility of the Interdisciplinary Center for Clinical Research (IZKF) Aachen for sequencing experiments. Special thanks go to Jasmin Hübner and Anna Rudzinski for their extraordinary help in sequencing the samples.

Conflicts of interest: Jonel Trebicka has received speaking and/or consulting fees from Astra-Zeneca, Gore, Boehringer-Ingelheim, Falk, Grifols, Genfit, and CSL Behring. T Bruns received consulting fees from Intercept/Advanz Pharma, Grifols, Sobi, and SmartDyeLivery. Paolo Caraceni has received speaking and/or consulting fees from Grifols SA , Octapharma SA, CSL Behring, and Gilead.

Data availability statement: Researchers who provide a methodology sound proposal can apply for the data, as far as the proposal is in line with the research consented by the patients. These proposals should be requested through https://www.clifresearch.com/decision/Home.aspx. Data requestors will need to sign a data transfer agreement.

Ethics approval statement: The studies involving human participants were reviewed and approved by the Ethical Board of all five participating centres in Europe. The patients/participants provided written informed consent to participate in this study.

Funding:
This project has received funding from the European Union's Horizon 2020 research and innovation program under grant agreement No 847949. This research was made possible through access to data generated by the PREDICT and ACLARA studies promoted and funded by the European Foundation for the Study of Chronic Liver Failure (EF-CLIF), a private, non-profit organization supported by unrestricted grants from Grifols and Genfit.

T.H.W. received financing from the START program of the RWTH Aachen University.

N.P.P. was funded by a Ramón y Cajal fellow (RYC2021-032197-I) from the MCIN/AEI/10.13039/501100011033 and European Union “NextGenerationEU”/PRTR and by a Juan de la Cierva-formación fellow (FJC2019-042304-I) from the Spanish Ministry of Science and Innovation (MCIN).

T.B. was supported by the German Research Foundation (SFB1383 Project ID 403224013/B07).

The Genome Analysis Platform in CIC bioGUNE is supported by the Basque Department of Industry, Tourism and Trade (Etortek, Elkartek and Emaitek Programs), the Innovation Technology Department of Bizkaia County, CIBERehd Network, and Spanish MINECO the Severo Ochoa Excellence Accreditation (CEX2021-001136-S).

JC laboratory is supported by Ministerio de Ciencia e Innovación/Agencia Estatal Investigación MCIN/AEI (PID2022-138970OB-I00 10.13039/501100011033/FEDER, UE). C.T. was supported by the DFG grants TR285/10-2 and SFB CRC1382, A08 (ID 403224013).

PER research laboratory is supported by the Fondation pour la Recherche Médicale (FRM EQU202303016287), “Institut National de la Santé et de la Recherche Médicale” (ATIP AVENIR), the “Agence Nationale pour la Recherche” (ANR-18-CE14-0006-01, RHU QUID-NASH, ANR-18-IDEX-0001,

ANR-22-CE14-0002) by « Émergence, Ville de Paris », by Fondation ARC and by France 2030 RHU LIVER-TRACK (ANR-23-RHUS-0014).

D.G.-C. research laboratory is supported by King Abdullah University of Science and Technology.

Authors´ contributions: THW, RK, JC, PER, CT, and DGC designed the study. THW, MRP, MB, GZ, DB, MS, WG, RS, SV, AV, DC, and IG supervised patient recruitment and sample collection and assessed clinical data. THW, MRP, FS, AMA, JR and LS performed experiments. SPE led and performed data assessment, analysis, and visualization. THW, DGC, NP, CLV and EH supported data assessment, analysis, and visualization. THW, SPE, MRP, LS, DGC, NP, EH performed data interpretation. THW, SPE, NP, and DGC wrote the manuscript. EH, MRP, FS, JR, AK, RK, TB, PC, CA, NK, LS, JT, JC, PER, and CT revised the manuscript. All authors provided intellectual input and approved the final version of the manuscript.

References

1. Ginès P, Krag A, Abraldes JG, Solà E, Fabrellas N, Kamath PS. Liver cirrhosis. The Lancet. 2021 Oct;398(10308):1359–76.
2. Mansour D, McPherson S. Management of decompensated cirrhosis. Clin Med (Lond). 2018 Apr 1;18(Suppl 2):s60–5.
3. Engelmann C, Clària J, Szabo G, Bosch J, Bernardi M. Pathophysiology of decompensated cirrhosis: Portal hypertension, circulatory dysfunction, inflammation, metabolism and mitochondrial dysfunction. Vol. 75, Journal of Hepatology. Elsevier B.V.; 2021. p. S49–66.
4. D'Amico G, Morabito A, D'Amico M, Pasta L, Malizia G, Rebora P, et al. Clinical states of cirrhosis and competing risks. J Hepatol. 2018 Mar;68(3):563–76.
5. Moreau R, Jalan R, Gines P, Pavesi M, Angeli P, Cordoba J, et al. Acute-on-chronic liver failure is a distinct syndrome that develops in patients with acute decompensation of cirrhosis. Gastroenterology. 2013 Jun;144(7):1426–37, 1437.e1-9.
6. Gustot T, Stadlbauer V, Laleman W, Alessandria C, Thursz M. Transition to decompensation and acute-on-chronic liver failure: Role of predisposing factors and precipitating events. J Hepatol. 2021 Jul;75 Suppl 1:S36–48.
7. Trebicka J, Fernandez J, Papp M, Caraceni P, Laleman W, Gambino C, et al. The PREDICT study uncovers three clinical courses of acutely decompensated cirrhosis that have distinct pathophysiology. J Hepatol. 2020 Oct 1;73(4):842–54.
8. Albillos A, Martin-Mateos R, Van der Merwe S, Wiest R, Jalan R, Álvarez-Mon M. Cirrhosis-associated immune dysfunction. Nat Rev Gastroenterol Hepatol. 2022 Feb;19(2):112–34.
9. Arroyo V, Angeli P, Moreau R, Jalan R, Clària J, Trebicka J, et al. The systemic inflammation hypothesis: Towards a new paradigm of acute decompensation and multiorgan failure in cirrhosis. J Hepatol. 2021 Mar;74(3):670–85.
10. Clària J, Arroyo V, Moreau R. Roles of systemic inflammatory and metabolic responses in the pathophysiology of acute-on-chronic liver failure. JHEP Reports. 2023 Sep;5(9):100807.
11. Clària J, Stauber RE, Coenraad MJ, Moreau R, Jalan R, Pavesi M, et al. Systemic inflammation in decompensated cirrhosis: Characterization and role in acute-on-chronic liver failure. Hepatology. 2016 Oct;64(4):1249–64.
12. Engelmann C, Sheikh M, Sharma S, Kondo T, Loeffler-Wirth H, Zheng YB, et al. Toll-like receptor 4 is a therapeutic target for prevention and treatment of liver failure. J Hepatol. 2020 Jul;73(1):102–12.
13. Clària J, Arroyo V, Moreau R. The Acute-on-Chronic Liver Failure Syndrome, or When the Innate Immune System Goes Astray. J Immunol. 2016 Nov 15;197(10):3755–61.
14. Trebicka J, Bork P, Krag A, Arumugam M. Utilizing the gut microbiome in decompensated cirrhosis and acute-on-chronic liver failure. Nat Rev Gastroenterol Hepatol. 2021 Mar;18(3):167–80.
15. Wasmuth HE, Kunz D, Yagmur E, Timmer-Stranghöner A, Vidacek D, Siewert E, et al. Patients with acute on chronic liver failure display "sepsis-like" immune paralysis. J Hepatol. 2005 Feb;42(2):195–201.
16. Martin-Mateos R, Alvarez-Mon M, Albillos A. Dysfunctional Immune Response in Acute-on-Chronic Liver Failure: It Takes Two to Tango. Front Immunol. 2019;10:973.
17. Weiss E, de la Grange P, Defaye M, Lozano JJ, Aguilar F, Hegde P, et al. Characterization of Blood Immune Cells in Patients With Decompensated Cirrhosis Including ACLF. Front Immunol. 2021 Feb 5;11.
18. Yao J, Liu T, Zhao Q, Ji Y, Bai J, Wang H, et al. Genetic landscape and immune mechanism of monocytes associated with the progression of acute-on-chronic liver failure. Hepatol Int. 2023 Jun 10;17(3):676–88.

883 19. Feio-Azevedo R, Boesch M, Radenkovic S, van Melkebeke L, Smets L, Wallays M, et al. Distinct
884 immunometabolic signatures in circulating immune cells define disease outcome in acute-on-
885 chronic liver failure. Hepatology. 2024 May 16;
886 20. Yao J, Ji Y, Liu T, Bai J, Wang H, Yao R, et al. Single-Cell RNA Sequencing Shows T-Cell Exhaustion
887 Landscape in the Peripheral Blood of Patients with Hepatitis B Virus-Associated Acute-on-
888 Chronic Liver Failure. Gut Liver. 2024 May 15;18(3):520–30.
889 21. Zhang P, Li H, Zhou C, Liu K, Peng B, She X, et al. Single-Cell RNA Transcriptomics Reveals the
890 State of Hepatic Lymphatic Endothelial Cells in Hepatitis B Virus-Related Acute-on-Chronic Liver
891 Failure. J Clin Med. 2022 May 20;11(10):2910.
892 22. Reyes M, Filbin MR, Bhattacharyya RP, Billman K, Eisenhaure T, Hung DT, et al. An immune-cell
893 signature of bacterial sepsis. Nat Med. 2020 Mar 17;26(3):333–40.
894 23. Bernsmeier C, Triantafyllou E, Brenig R, Lebosse FJ, Singanayagam A, Patel VC, et al. CD14+
895 CD15- HLA-DR- myeloid-derived suppressor cells impair antimicrobial responses in patients
896 with acute-on-chronic liver failure. Gut. 2018 Jun;67(6):1155–67.
897 24. Bernsmeier C, Pop OT, Singanayagam A, Triantafyllou E, Patel VC, Weston CJ, et al. Patients
898 with acute-on-chronic liver failure have increased numbers of regulatory immune cells
899 expressing the receptor tyrosine kinase MERTK. Gastroenterology. 2015 Mar;148(3):603-
900 615.e14.
901 25. Yao RQ, Zhao PY, Li ZX, Liu YY, Zheng LY, Duan Y, et al. Single-cell transcriptome profiling of
902 sepsis identifies HLA-DRlowS100Ahigh monocytes with immunosuppressive function. Mil Med
903 Res. 2023 Jun 19;10(1):27.
904 26. von Baehr V, Döcke WD, Plauth M, Liebenthal C, Küpferling S, Lochs H, et al. Mechanisms of
905 endotoxin tolerance in patients with alcoholic liver cirrhosis: role of interleukin 10, interleukin
906 1 receptor antagonist, and soluble tumour necrosis factor receptors as well as effector cell
907 desensitisation. Gut. 2000 Aug;47(2):281–7.
908 27. Cheng SC, Scicluna BP, Arts RJW, Gresnigt MS, Lachmandas E, Giamarellos-Bourboulis EJ, et al.
909 Broad defects in the energy metabolism of leukocytes underlie immunoparalysis in sepsis. Nat
910 Immunol. 2016 Apr 7;17(4):406–13.
911 28. Li J, Liang X, Jiang J, Yang L, Xin J, Shi D, et al. PBMC transcriptomics identifies immune-
912 metabolism disorder during the development of HBV-ACLF. Gut. 2022 Jan;71(1):163–75.
913 29. Maheshwari D, Kumar D, Jagdish RK, Nautiyal N, Hidam A, Kumari R, et al. Bioenergetic Failure
914 Drives Functional Exhaustion of Monocytes in Acute-on-Chronic Liver Failure. Front Immunol.
915 2022 Jun 3;13.
916 30. Langer MM, Eickelmann C, Kleinbongard P, Lange CM. Impaired mitochondrial complex IV
917 respiration in peripheral blood mononuclear cells discriminates acute-on-chronic liver failure
918 from acute decompensation. J Hepatol. 2022 Sep;77(3):874–6.
919 31. Zhang IW, Curto A, López-Vicario C, Casulleras M, Duran-Güell M, Flores-Costa R, et al.
920 Mitochondrial dysfunction governs immunometabolism in leukocytes of patients with acute-
921 on-chronic liver failure. J Hepatol. 2022 Jan;76(1):93–106.
922 32. Wasmuth HE, Kunz D, Yagmur E, Timmer-Stranghöner A, Vidacek D, Siewert E, et al. Patients
923 with acute on chronic liver failure display "sepsis-like" immune paralysis. J Hepatol. 2005
924 Feb;42(2):195–201.
925 33. Bernsmeier C, van der Merwe S, Périanin A. Innate immune cells in cirrhosis. J Hepatol. 2020
926 Jul;73(1):186–201.
927 34. Bajaj JS, Salzman NH, Acharya C, Sterling RK, White MB, Gavis EA, et al. Fecal Microbial
928 Transplant Capsules Are Safe in Hepatic Encephalopathy: A Phase 1, Randomized, Placebo-
929 Controlled Trial. Hepatology. 2019 Nov;70(5):1690–703.
930 35. Trebicka J, Macnaughtan J, Schnabl B, Shawcross DL, Bajaj JS. The microbiota in cirrhosis and
931 its role in hepatic decompensation. J Hepatol. 2021 Jul;75 Suppl 1(Suppl 1):S67–81.

932 36. Ruitenberg JJ, Mulder CB, Maino VC, Landay AL, Ghanekar SA. VACUTAINER CPT and Ficoll
933 density gradient separation perform equivalently in maintaining the quality and function of
934 PBMC from HIV seropositive blood samples. BMC Immunol. 2006 May 25;7:11.
935 37. Zheng GXY, Terry JM, Belgrader P, Ryvkin P, Bent ZW, Wilson R, et al. Massively parallel digital
936 transcriptional profiling of single cells. Nat Commun. 2017 Jan 16;8(1):14049.
937 38. Dobin A, Davis CA, Schlesinger F, Drenkow J, Zaleski C, Jha S, et al. STAR: ultrafast universal
938 RNA-seq aligner. Bioinformatics. 2013 Jan 1;29(1):15–21.
939 39. Hao Y, Hao S, Andersen-Nissen E, Mauck WM, Zheng S, Butler A, et al. Integrated analysis of
940 multimodal single-cell data. Cell. 2021 Jun;184(13):3573-3587.e29.
941 40. Hafemeister C, Satija R. Normalization and variance stabilization of single-cell RNA-seq data
942 using regularized negative binomial regression. Genome Biol. 2019 Dec 23;20(1):296.
943 41. Butler A, Hoffman P, Smibert P, Papalexi E, Satija R. Integrating single-cell transcriptomic data
944 across different conditions, technologies, and species. Nat Biotechnol. 2018 May 2;36(5):411–
945 20.
946 42. Korsunsky I, Millard N, Fan J, Slowikowski K, Zhang F, Wei K, et al. Fast, sensitive and accurate
947 integration of single-cell data with Harmony. Nat Methods. 2019 Dec 18;16(12):1289–96.
948 43. Mulè MP, Martins AJ, Tsang JS. Normalizing and denoising protein expression data from
949 droplet-based single cell profiling. Nat Commun. 2022 Apr 19;13(1):2099.
950 44. Miller SA, Policastro RA, Sriramkumar S, Lai T, Huntington TD, Ladaika CA, et al. LSD1 and
951 Aberrant DNA Methylation Mediate Persistence of Enteroendocrine Progenitors That Support
952 *BRAF* -Mutant Colorectal Cancer. Cancer Res. 2021 Jul 15;81(14):3791–805.
953 45. Wu T, Hu E, Xu S, Chen M, Guo P, Dai Z, et al. clusterProfiler 4.0: A universal enrichment tool
954 for interpreting omics data. The Innovation. 2021 Aug;2(3):100141.
955 46. Qiu X, Mao Q, Tang Y, Wang L, Chawla R, Pliner HA, et al. Reversed graph embedding resolves
956 complex single-cell trajectories. Nat Methods. 2017 Oct 21;14(10):979–82.
957 47. Andrews S. http://www.bioinformatics.babraham.ac.uk/projects/fastqc. 2010. FastQC: a
958 quality control tool for high throughput sequence data.
959 48. Bolger AM, Lohse M, Usadel B. Trimmomatic: a flexible trimmer for Illumina sequence data.
960 Bioinformatics. 2014 Aug 1;30(15):2114–20.
961 49. Anders S, Pyl PT, Huber W. HTSeq—a Python framework to work with high-throughput
962 sequencing data. Bioinformatics. 2015 Jan 15;31(2):166–9.
963 50. Law CW, Chen Y, Shi W, Smyth GK. voom: precision weights unlock linear model analysis tools
964 for RNA-seq read counts. Genome Biol. 2014;15(2):R29.
965 51. Hänzelmann S, Castelo R, Guinney J. GSVA: gene set variation analysis for microarray and RNA-
966 Seq data. BMC Bioinformatics. 2013 Dec 16;14(1):7.
967 52. Farias AQ, Curto Vilalta A, Momoyo Zitelli P, Pereira G, Goncalves LL, Torre A, et al. Genetic
968 Ancestry, Race, and Severity of Acutely Decompensated Cirrhosis in Latin America.
969 Gastroenterology. 2023 Sep;165(3):696–716.
970 53. Robin X, Turck N, Hainard A, Tiberti N, Lisacek F, Sanchez JC, et al. pROC: an open-source
971 package for R and S+ to analyze and compare ROC curves. BMC Bioinformatics. 2011 Dec
972 17;12(1):77.
973 54. Hajian-Tilaki K. Receiver Operating Characteristic (ROC) Curve Analysis for Medical Diagnostic
974 Test Evaluation. Caspian J Intern Med. 2013;4(2):627–35.
975 55. Acin-Perez R, Benador IY, Petcherski A, Veliova M, Benavides GA, Lagarrigue S, et al. A novel
976 approach to measure mitochondrial respiration in frozen biological samples. EMBO J. 2020 Jul
977 1;39(13):e104073.
978 56. R Core Team. R: A language and environment for statistical computing. Vienna, Austria: R
979 Foundation for Statistical Computing; 2021.
980

981

982

983 **Table**

984

985 ***Table 1. Baseline characteristics of single-cell study cohort.***

	HC (n=4)	SDC (n=6)	UDC (n=6)	pre-ACLF (n=4)	*p*-value
Characteristics					
Age, median (range)	56 (52 - 64)	60 (54 - 81)	57 (51- 60)	74 (60 - 79)	0.063
Female Sex, yes, n (%)	2 (50)	2 (33)	0	2 (50)	0.248
Previous decompensations in the last 2 years, yes, n (%)	-	0	4 (67)	3 (75)	**0.023**
Cause of cirrhosis, n (%)					
Alcohol-related	-	1 (17)	3 (50)	2 (50)	0.606
Viral (HBV/HCV)	-	1 (17)	1 (17)	0	0.259
Alcohol-related + MASLD	-	1 (17)	1 (17)	0	0.259
MASLD	-	2 (50)	1 (17)	1 (25)	0.801
cryptogenic	-	0	0	1 (25)	0.202
other	-	1 (17)	0	0	0.411
Data at admission, n (%)					
Ascites	-	5 (83)	5 (83)	4 (100)	0.683
SBP	-	0	0	2 (50)	**0.032**
Other bacterial infection	-	2 (33)	0	0	0.149
Variceal bleeding	-	0	1 (17)	0	0.411
HE	-	1 (17)	2 (33)	1 (25)	0.801
Alcoholic hepatitis		1 (17)	0	1 (25)	0.467
Acute kidney injury	-	0	1 (17)	0	0.411
Laboratory parameters					
Bilirubin, total [mg/dl], median, (range)	-	2.31 (1.3-3.4)	2.14 (1.37-4.60)	3.91 (2.61-5.85)	0.217
AST [U/l], median, (range)		44 (28-64)	61 (35-361)	54 (34-125)	0.294
ALT [U/l], median, (range)		33 (11-38)	32 (17-76)	36 (18-57)	0.709
INR, median, (range)		1.38 (1.20-1.75)	1.46 (1.31-1.77)	1.69 (1.26-2.95)	0.516
Creatinine [mg/dl], median, (range)		0.72 (0.54-0.92)	0.80 (0.60-1.97)	1.36 (1.17-1.62)	**0.012**
Platelets [$x10^3$/L], median (range)		79 (39-176)	75 (41-130)	81 (37-106)	0.972
WBC [$x10^9$/L], median (range)	4.8 (4.0-6.3)	4.1 (2.1-5.7)	5.4 (2.9-7.5)	5.5 (3.4-9.4)	0.476
CRP [mg/L], median (range)	-	16.25 (2.22-76)	13.7 (1.78-45.2)	8.55 (1.23-37.10)	0.567
Severity scores					
Child-Pugh, median, range	-	7.5 (5 - 12)	10 (7 - 11)	11 (8 - 13)	0.126
MELD, median, range	-	12 (8 - 18)	13 (12 - 23)	20 (17 - 27)	**0.033**
CLIF-C AD, median, range	-	47 (41 - 49)	47.5 (41 - 59)	61 (55 - 74)	**0.025**
Treatment at blood draw					
Diuretics, yes, n (%)	-	3 (50)	4 (67)	3 (75)	0.701
Antibiotics, yes, n (%)	-	1 (17)	1 (17)	1 (25)	0.934
Non-selective ß-blockers, yes, n (%)	-	1 (17)	2 (33)	3 (75)	0.169
Albumin, yes, n (%)	-	1 (17)	0	1 (25)	0.467
HE treatment, yes, n (%)	-	1 (17)	3 (50)	3 (75)	0.176

Follow-up and Outcome					
90-day mortality, yes, n (%)	-	0	0	1 (25)	0.229
90-day OLT, yes, n (%)	-	0	0	1 (25)	0.229

986 HE treatment includes lactulose and rifaximin. Baseline characteristics are depicted as frequencies or median
987 (IQR). Values of *p*-value are based on Wilcoxon–Mann–Whitney test for continuous and chi-square test for
988 categorical variables. *Abbreviations:* SDC, stable decompensated cirrhosis; UDC, unstable decompensated
989 cirrhosis; pre-ACLF, pre-acute-on-chronic liver failure; HBV, Hepatitis B virus; HCV, Hepatitis C virus; MASLD,
990 metabolic-dysfunction associated steatotic liver disease; SBP, spontaneous bacterial peritonitis; HE, hepatic
991 encephalopathy; AST, aspartate aminotransferase; ALT, alanine aminotransferase; WBC, white blood cell
992 count; CRP, C-reactive protein; OLT, orthotopic liver transplantation.
993

994

995